A&A 580, A42 (2015)
DOI: 10.1051/0004-6361/201425535

Astronomy & Astrophysics

Emission-line-selected galaxies at z = 0.6–2 in GOODS South: Stellar masses, SFRs, and large-scale structure⋆

I. Kochiashvili[1,2], P. Møller[3], B. Milvang-Jensen[1], L. Christensen[1], J. P. U. Fynbo[1], W. Freudling[3], B. Clément[4,5], J.-G. Cuby[6], J. Zabl[1], and S. Zibetti[7]

[1] Dark Cosmology Centre, Niels Bohr Institute, University of Copenhagen, Juliane Maries Vej 30, 2100 Copenhagen Ø, Denmark
e-mail: ia@dark-cosmology.dk
[2] Abastumani Astrophysical Observatory, Ilia State University, Kakutsa Cholokashvili Ave 3/5, 0162 Tbilisi, Georgia
[3] European Southern Observatory, Karl Schwarzschild Strasse 2, 85748 Garching bei München, Germany
[4] Steward Observatory, University of Arizona, 933 North Cherry Avenue, Tucson, AZ, 85721, USA
[5] CRAL, Observatoire de Lyon, Université Lyon 1, 9 avenue Ch. André, 69561 Saint Genis Laval Cedex, France
[6] Aix Marseille Université, CNRS, LAM (Laboratoire d'Astrophysique de Marseille) UMR 7326, 13388 Marseille, France
[7] INAF–Osservatorio Astrofisico di Arcetri, Largo Enrico Fermi 5, 50125 Firenze, Italy

Received 17 December 2014 / Accepted 10 April 2015

ABSTRACT

We have obtained deep NIR narrow and broad (J and Y) band imaging data of the GOODS-South field. The narrow band filter is centered at 1060 nm corresponding to redshifts z = 0.62, 1.15, 1.85 for the strong emission lines Hα, [OIII]/Hβ and [OII], respectively. From those data we extract a well defined sample (M(AB) = 24.8 in the narrow band) of objects with large emission line equivalent widths in the narrow band. Via SED fits to published broad band data we identify which of the three lines we have detected and assign redshifts accordingly. This results in a well defined, strong emission line selected sample of galaxies down to lower masses than can easily be obtained with only continuum flux limited selection techniques. We compare the (SED fitting-derived) main sequence of star-formation (MS) of our sample to previous works and find that it has a steeper slope than that of samples of more massive galaxies. We conclude that the MS steepens at lower (below $M_\star = 10^{9.4}\ M_\odot$) galaxy masses. We also show that the SFR at any redshift is higher in our sample. We attribute this to the targeted selection of galaxies with large emission line equivalent widths, and conclude that our sample forms the upper boundary of the MS. We briefly investigate and outline how samples with accurate redshifts down to those low stellar masses open a new window to study the formation of large scale structure in the early universe. In particular we report on the detection of a young galaxy cluster at z = 1.85 which features a central massive galaxy which is the candidate of an early stage cD galaxy, and we identify a likely filament mapped out by [OIII] and Hβ emitting galaxies at z = 1.15.

Key words. galaxies: high-redshift

1. Introduction

The study of galaxies at both intermediate and high redshifts has gained tremendous momentum from the concerted efforts to gather deep imaging of large fields and from the ensuing high-quality photometry covering broad spectral ranges. Analyses exploiting those data to derive prime observables such as star-formation rates (SFRs) and stellar masses $M_\star$ have revealed that galaxies follow scaling relations that evolve with redshifts (Brinchmann et al. 2004; Noeske et al. 2007; Daddi et al. 2007). The most comprehensive investigations are based on multi-band photometry, and the ability to obtain redshift information by fitting theoretical model data is a critical component (Daddi et al. 2007; Karim et al. 2011; Bayliss et al. 2011; Koyama et al. 2013). The photometric redshift accuracy also places a fundamental limitation on the results from the unavoidable uncertainty in the assignment of redshifts to each galaxy, an uncertainty that propagates to all the derived physical parameters of the galaxies.

There are different methods of addressing the galaxy formation and evolution quest. Galaxy samples are selected differently and therefore probe different aspects of galaxy evolution. Intensively star-forming galaxies have been studied for nearly two decades with the help of the Lyman-break selection technique (Steidel et al. 2003; Shapley 2011). Flux limited high-redshift samples selected at primarily red wavelengths include luminous infrared galaxies (LIRGs), ultra luminous infrared galaxies (ULIRGs), and massive ($M_\star \sim 10^{10.7}\ M_\odot$) red ellipticals (Jacobs et al. 2011). Sub-millimetre selected samples target high-redshift galaxies with unprecedented star-formation rates (Michałowski et al. 2010; Hodge et al. 2013). Long-duration gamma-ray bursts (GRBs) select fainter and bluer star-forming galaxies (Le Floc'h et al. 2003; Christensen et al. 2004). Also selection effects play a role here, because it has been suggested that GRB hosts have to have low stellar masses (e.g. Castro Cerón et al. 2010), while dusty GRBs occur primarily in more massive host galaxies (Krühler et al. 2011). Absorption-line selected samples allow us to study the gas content of galaxies and can be used to probe the mass-metallicity relation (Ledoux et al. 2006; Møller et al. 2013; Christensen et al. 2014). In a nutshell, these methods all address different populations of galaxies and have different advantages and disadvantages for particular science goals.

To investigate the $M_\star$ vs. SFR relation for galaxies found in isolation and in clusters, none of these methods will simultaneously probe the low-mass end of the star-forming main sequence and cover intermediate-to-high redshifts. An alternative

⋆ Tables 1 and 2, and Appendix A are available in electronic form at http://www.aanda.org

method that can help us in achieving this goal is the narrow-band imaging technique (e.g. Pritchet & Hartwick 1987). Emission-line-selected samples are smaller, but the advantage is that they allow us to probe fainter objects than broad-band-selected samples do and still have a much more accurate photometric redshift determination (Ly et al. 2012; Sobral et al. 2014). Narrow-band selected objects have excess flux in the narrow-band filter compared to a broad-band filter that covers adjacent wavelengths. Primarily, this technique has been used to detect high-redshift Lyman-α (Lyα) emission lines because Lyα is a good tracer of galaxies at the beginning of the reionization era (Partridge & Peebles 1967; Malhotra & Rhoads 2004; Nilsson et al. 2007).

The goal of this paper is to fill in the knowledge gap concerning the low-mass end of the main sequence of star-forming galaxies in a broad redshift range. We have analysed emission-line sources selected from deep 1060 nm narrow-band ($NB1060$ hereafter) and Y- and J-band observations of the GOODS-South field from Clément et al. (2012). The GOODS-South field is ideal for our objective because the field has been observed in a wide range of wavelengths and with good photometric accuracy (Giavalisco et al. 2004) allowing for very detailed photometric scrutiny of sources in the field. When searching for emission-line galaxies at redshifts $z \sim 7.7$, we also detect galaxies with emission lines other than Lyα falling within the narrow-band filter. In this way, we can probe the universe in four independent redshift slices: besides the high-redshift Lyα line, we detect galaxies at $z = 0.6$ from strong Hα emission lines, at $z = 1.12/1.18$ from [OIII]/Hβ emission lines, and $z = 1.85$ where galaxies with strong [OII] emission lines lie. We performed multi-band photometry SED fitting and derived masses and SFRs of 40 emission-line galaxies at three different redshift slices. We analysed the redshift evolution of the $M_\star$–SFR relation spanning more than four decades in stellar mass from a unique data set.

The paper is organized as follows. In Sect. 2 we describe candidate-selection process and the datasets used for this project. Section 3 characterizes the spectroscopic and photometric properties of the selected galaxies and compare with redshifts from the MUSYC survey. Sections 4 and 5 present the results anddiscusses these.

Throughout this paper, we assume a flat cosmology with $\Omega_\Lambda = 0.70$, $\Omega_\mathrm{m} = 0.30$, and a Hubble constant of $H_0 = 70$ km s^{-1} Mpc^{-1}.

2. Selection of emission-line galaxies

2.1. Imaging observations

The GOODS South field was observed with VLT/HAWK-I in the 1060 nm narrow-band and broad J- and Y-band filters (see filter transmission curves in Fig. 1) as part of a Large ESO Programme (Prog-Id: 181.A-0485, PI: Cuby) and a HAWK-I science verification programme (Prog-Id: 60.A-9284(B), PI: Fontana). For details on the observations and data reduction we refer to Castellano et al. (2010) and Clément et al. (2012). The field is in the northern half of the GOODS-S field (centred at RA, Dec = $03^\mathrm{h}32^\mathrm{m}29^\mathrm{s}$, $-27^\mathrm{d}44^\mathrm{m}42^\mathrm{s}$, J2000).

2.2. Candidate selection

For object detection and photometry, we used the software package SExtractor (Bertin & Arnouts 1996). For the actual selection of candidate emission line galaxies we only relied on the Hawk-I $NB1060$, Y and J-band images. As a detection image we use the narrow-band image, and photometry is subsequently done in all three images with aperture sizes defined in the $NB1060$ image. Before object detection the detection image is convolved with a Gaussian filter function having a FWHM equal to that of point sources. We used a detection threshold of 1.5 times the background sky-noise in the unfiltered detection image and a minimum area of 15 connected pixels above the detection threshold in the filtered image. Isophotal apertures are defined on the detection image and those same isophotal apertures are used in the different bands ($NB1060$, Y, J). We rejected objects close to the chip gap and the edge of the image where the noise is higher. The regions of the field masked out in this way are shown in Fig. 15. In total, we detect 2700 objects at a signal-to-noise ratio greater than 5 in the narrow-band. We measured the flux of all objects in the isophotal aperture that is suitable for precise colour measurement since the effective seeing of the images are very similar. To have a measure of the total magnitudes, we used the so-called AUTO aperture in SExtractor. The AUTO aperture is an elliptical aperture defined by the isophotal shape of the object. For objects blended with neighbours a scaled isophotal flux is used to estimate the total flux. Our final catalogue is complete (10σ detection) down to $M(\mathrm{AB}) = 24.8$ in the narrow-band.

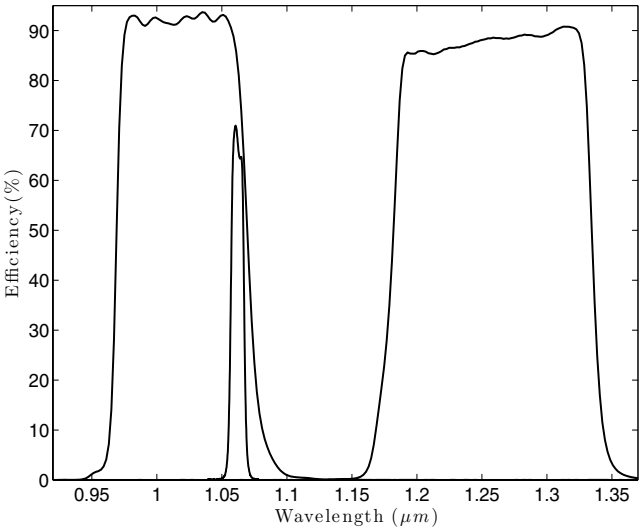

Fig. 1. Transmission curves for the $NB1060$, Y, and J-band filters. The narrow filter transmission is located in the red wing of the Y-band filter and is entirely outside the J-band transmission range.

To select objects with excess flux in the narrow-band, we employed the method introduced by Møller & Warren (1993) and refined by Fynbo et al. (2003). This method uses two broad band filters that bracket the narrow band. Plotting the two narrow-minus-broad colours against each other causes objects with an emission line within the narrow pass band to drop diagonally down to the left (Fig. 2 upper panel). We computed the distribution of the cloud of continuum emitters using theoretical spectral energy distributions from Bruzual & Charlot (2003), and enclosed the region where the model galaxies fall in Fig. 2 (for details see Fynbo et al. 2003). All objects in our catalogue are plotted in the upper panel of Fig. 2, and it is seen that most objects do indeed fall inside the red dashed line. The selection window we have adopted is seen below and to the left side of the main locus of continuum objects. For $NB1060 - J < -1$, we selected objects with $NB1060 - Y < -0.2$. For $NB1060 - J > -1$ we use $NB1060 - Y < -0.7 \times (NB1060 - J) - 0.9$. The 40 objects found inside this area and, at least 1σ from the border, make up our "basic sample" and are listed in Table 1 and are highlighted

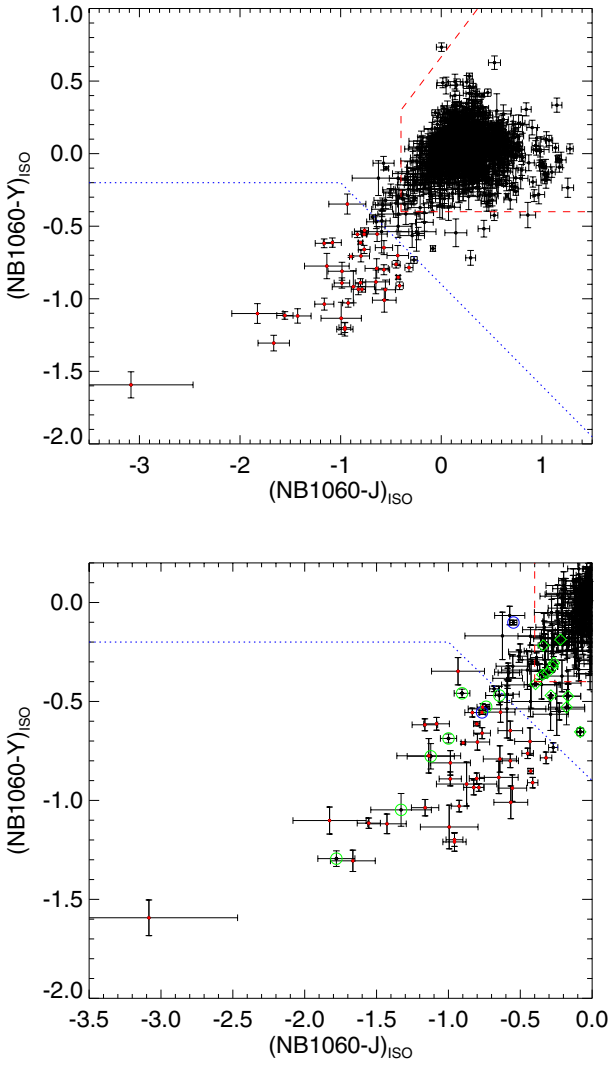

Fig. 2. Colour–colour diagram for objects detected in the *NB1060* image and brighter than NB1060(AUTO) = 24.8. The *top panel* represents the colour distribution of continuum and emission-line galaxies. The expected region occupied by continuum emitters is enclosed by a red dashed line, whereas the region we use to select candidate line emitters lies below the blue dotted line. Red dots represent objects from the basic sample, i.e. objects that meet the selection criteria. The *lower panel* additionally shows objects in green circles and green diamonds that have emission-lines but do not enter our basic sample because they either are masked or lie outside a conservatively defined selection area (therefore above the blue dotted line).

in Fig. 2. The basic sample is complete in that we have included all objects within the unmasked area of the observed field down to $NB1060 = 24.8$, and it is therefore suitable for statistical studies within the unmasked area that spans 38.7 square arcminutes on the sky.

We searched the NED/IPAC[1] and SIMBAD (Wenger et al. 2007) databases and found spectroscopic, secure redshifts for a subset of the basic sample, as listed in Table 1.

As a check of the selection, the images were inspected in ds9 in RGB mode, with blue = Y, green = *NB1060*, red = J. Objects were marked that looked green (i.e. showed some degree of narrow-band excess) and which looked like galaxies and not artifacts or noise. The mask used in defining the basic sample was not used, i.e. also objects located in higher noise regions of the image were included. After removing the basic sample of 40 galaxies and the ELG00 galaxy, this visually-identified narrow-band excess sample comprised 58 objects. There were three not necessarily mutually exclusive reasons for these galaxies not being part of the basic sample: (1) their colours were outside the selection region i.e. the observed EW was too low; (2) they were in a masked part of the image; or (3) they were fainter than *NB1060*(AUTO) = 24.8. SIMBAD was searched, and 18 of the 58 objects had a spectroscopic, secure redshift. For all 18 galaxies (named x01 to x18), the redshift matched an emission line (see Table 2). These 18 galaxies, as well as ELG00 (see below), do not fulfil our selection criteria and thus cannot be used in our basic sample, but together with the basic sample they form an "extended sample".

In addition we obtained spectra and determined redshifts for two objects as described in Sect. 3.1. The two objects are highlighted by blue circles in Fig. 2, where one is seen to be in our basic sample (ELG55) while the other is directly to the left of the large cloud of galaxies. This is an intriguingly strange position since it shows that it has an emission line in the $(NB1060 - J)$ colour, but no line in the $(NB1060 - Y)$ colour. It is not in the basic sample, so we have named it ELG00 and list it in the first line of Table 2.

In Fig. A.1 we show *NB*1060, *Y* and HST *F606W*-band thumbnails (the last is the deepest optical band we have) for all 40 galaxies in the basic sample, and also including ELG00 of the extended sample. As seen, all are indeed detected in the *F606W*-band so are not consistent with being Lyα emitters at $z = 7.7$. The candidates have very mixed morphologies ranging from bright spirals over irregular galaxies with multiple cores to very faint compact systems.

3. Characterization of the candidate emission-line galaxies

3.1. Spectroscopic observations

On March 15 and 16, 2013 we secured redshift measurements for two objects in our catalogue. The spectra were obtained with the X-Shooter spectrograph (Vernet et al. 2011) installed at the Cassegrain focus of the Very Large Telescope (VLT), Unit 2 – Kueyen, operated by the European Southern Observatory (ESO) on Cerro Paranal in Chile (prog. ID 090.A-0147). The spectra were reduced with the ESO X-Shooter pipeline 2.0 (Goldoni 2011). In Fig. 3 we show the X-Shooter spectra around the region of the *NB*1060 filter.

One of the object (ELG55, lower panel of Fig. 3) belongs to the basic sample, and we see that the line is confirmed to [OIII]λ5007 based on the detection of [OIII]λ4959 and [OII]λ3727, and the derived redshift is 1.1107.

The other object (ELG00, upper panel of Fig. 3) is not in the basic sample but was observed because of its strange position in the colour-colour plot as described in Sect. 2.2 above. Here we see a strong Hα line (based on the detection of a wide range of other lines in the visual spectral region) and the derived redshift is 0.6045. The strong Hα line is located in the very wing of the filter curve as given by the ESO web page[2] We do not detect the [NII]λ6583 line in the spectrum.

[1] The NASA/IPAC Extragalactic Database (NED) is operated by the Jet Propulsion Laboratory, California Institute of Technology, under contract with the National Aeronautics and Space Administration.

[2] http://www.eso.org/sci/facilities/paranal/instruments/hawki/inst/filters/hawki_NB1060.dat

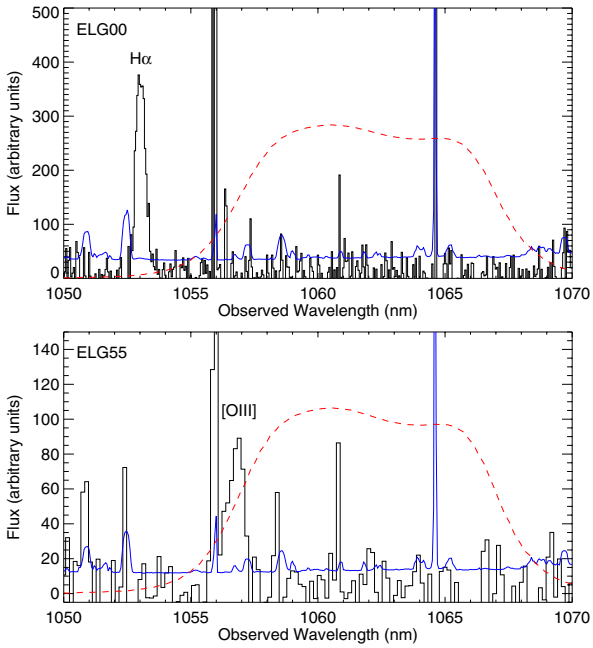

Fig. 3. X-Shooter spectra of ELG00 (*top*) and ELG55 (*bottom*). The red dashed line shows the *NB1060* filter transmission curve, the blue solid line is the error spectrum. Hα of ELG00 is seen to be out of the narrow band pass transmission causing its peculiar colours.

3.2. Photometric redshifts

The very conservative selection criteria employed for our basic sample definition ensures that a strong emission line is present in the narrow-band filter. Therefore the task of redshift determination of our narrow-band-selected sample is reduced to determining which of the three most likely redshift groups each object belongs to, Hα, [OIII]/Hβ, or [OII]. In a few cases we already have spectroscopic confirmations, and for the remainder we rely on photometric redshift analysis. For this we take advantage of the variety of photometric data available for the GOODS field. We explored a wide range of available data sets, and in the end we concluded that the most robust results are obtained primarily using the available photometry from the CANDELS survey (Guo et al. 2013) (G13 hereafter). This survey includes nearly 35 000 sources that combine data from among others HST-WFC3 and HST-ACS, VLT-VIMOS, VLT-HawkI, VLT-ISAAC and Spitzer/IRAC, spanning wavelengths from the UV to the near-infrared. The CANDELS catalogue contains magnitudes and magnitude errors for 17 different bands in total. To construct the catalogue, a careful and complete source detection algorithm, as well as flux derivation methods including aperture corrections, were employed. However, no photometric or spectroscopic redshift information is provided in the catalogue.

Y-band photometry was not available in G13 for a subset of objects (the last 14 in Table 1). For these targets we added our own *Y*-band photometry (from HAWK-I) to the data sets before the SED fitting and redshift determination. For these objects we performed aperture photometry in circular apertures. The aperture size was matched to the apparent extension of the object on the sky. For each used aperture size, we determined aperture corrections measured on isolated, unsaturated point sources.

For the spectral energy distribution (SED) fits we use the LePhare code (Arnouts et al. 1999; Ilbert et al. 2006). Those fits also provide a first photometric redshift probability distribution, which we use to guide us towards the final "redshift slice" assignments for each object.

To construct the model SED, we used the Bruzual and Charlot (BC03) spectral library (Bruzual & Charlot 2003). The library uses stellar evolutionary tracks for different metallicities and helium abundances from the Padova 1994 stellar synthesis models. It generates spectra in the wavelength range from 3200 to 9500 Å at higher resolution and across a wider wavelength range, 91 Å to 160 μm with lower resolution, assuming Chabrier initial mass function (IMF) (Chabrier 2003) and the Calzetti extinction law (Calzetti et al. 2000). The ages for the model galaxies range from 10^5 to 2×10^{10} yr. The code is based on the exponentially declining star formation history (SFH). We also include contribution from the emission lines in the models. For this, LePhare uses a simple recipe based on the Kennicutt (1998) SFR and UV luminosity relation. The code includes the strongest emission such as the Lyα, Hα, Hβ, [OIII] doublet – $\lambda\lambda$4959, 5007 Å and [OII], varying the ratio of the above-mentioned lines with [OII]. For further details on LePhare code characteristics, see Ilbert et al. (2006) and the LePhare manual.

For each object we go through the following steps. We fit an SED to the full set of photometric data twice, once using all data points and once where we exclude the narrow band and the *Y* band since they are both dominated by the emission line, which may skew the fit. We then decide, after visual inspection of each individual fit, whether there is a unique solution or if two or even all three redshift solutions are possible. This is done independently by four of us and redshifts are only assigned if we all four agree. For most (35) objects there clearly is a unique solution, but for the remaining five objects, no unique redshift assignment is possible this way. In four cases there is a best solution (dubbed "primary redshift" and listed first in Table 1) but also a possible secondary solution. In one case (ELG30), all three solutions are possible but none of them are preferred. ELG30 is the object that is in the lowest left-hand corner of Fig. 2, that is, it has larger emission line equivalent width than any other object in our sample. Presumably the strong emission lines are confusing the SED fit. All redshifts assigned in this way are provided in Table 1. As a final step we then repeat the SED fit but this time locking the redshift to the spectroscopic redshift (when available) or to the assigned redshift based on the identification of the emission line. The purpose of this last fit is to obtain the best-fitted values for stellar mass and star formation rate.

In Fig. 4 we show examples of fits to three of the objects with unique solutions, one belonging to each redshift slice. We show both the first fit where the redshift was left as a free parameter, and the final fit with assigned redshift.

3.2.1. The $V-I$ vs. $Z-J$ redshift diagnostic plot

In Fig. 6 we plot the $V - I$ colour versus the $Z - J$ colour for all the unique object redshifts and the four primary but non-unique redshift solutions. The objects are colour-coded according to redshift slice (Hα blue, [OIII]/Hβ green, and [OII] red). It is seen that the points separate out quite clearly in this diagram, in agreement with the work by Bayliss et al. (2011). Galaxies move from the lower right towards the upper left in this diagram as they move to lower redshifts, and it is a coincidence that the internal scatter of the distribution at any given redshift forms a perfect match to the separation in redshift forced by the wavelengths of the three transitions. It is therefore possible to

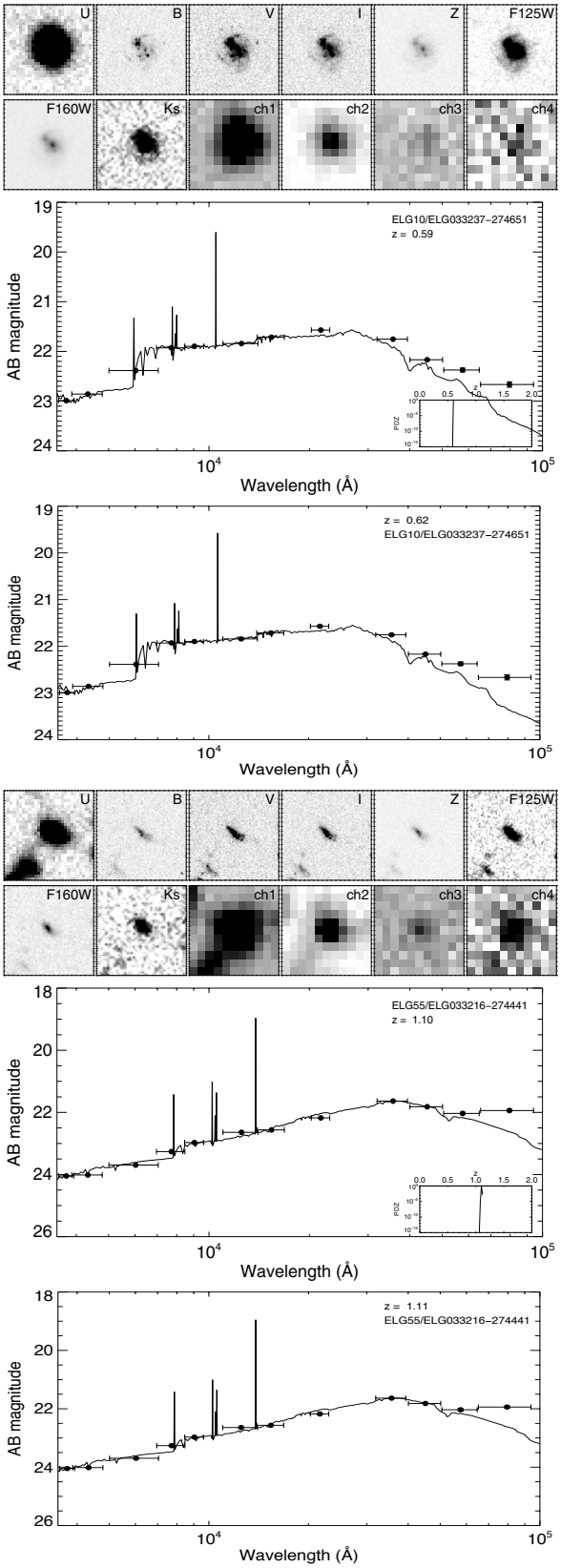

Fig. 4. Illustration of our redshift assignment procedure, we show an example for each z slice. We first fit the SED leaving z as a free parameter (upper fit for each slice), based on the z-probability density from that fit we then assign a slice and fit for that z value (lower fit for each slice). We also provide thumbnail images covering 6×6 arcsec^2 around each object in broad band filter images from U through *Spitzer* channel 4. Errors on the photometry are included in the figure, but are in almost all cases too small to be visible.

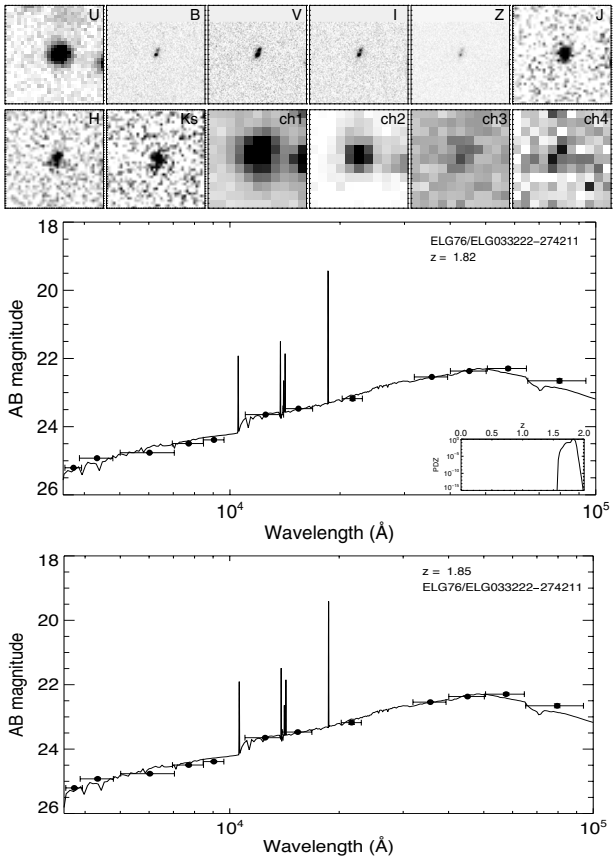

Fig. 4. continued.

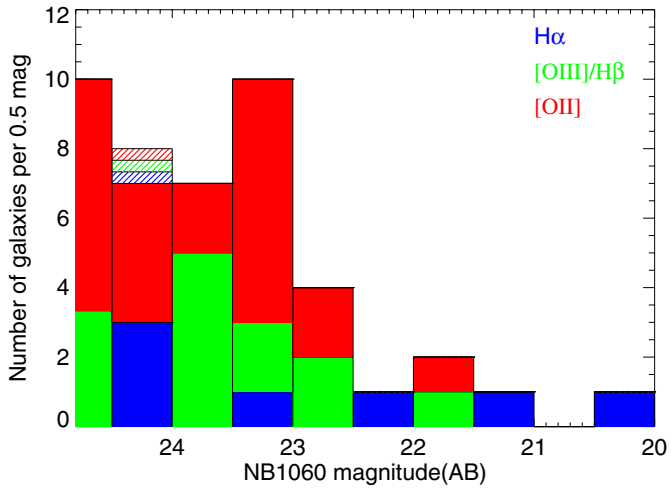

Fig. 5. Emission-line flux distribution of objects in our three redshift slices. It is seen that the median narrow-band magnitude is roughly 23.5 for all slices. ELG 30 is indicated as the hashed object with undecided redshift. The last bin size ($M_{\rm AB} > 24.5$) is 0.3 instead of 0.5 and has been scaled accordingly.

use this figure as a diagnostic plot to assist slice identification in cases where no unique solution can be found. Our primary redshifts are seen to agree well with this plot, which is further proof that those assignments are correct. We also plotted the last object without redshift assignment (ELG30), and we see that it is mostly embedded in the region occupied by [OII] emitters, also close to [OIII] emitters, but far away from Hα emitters.

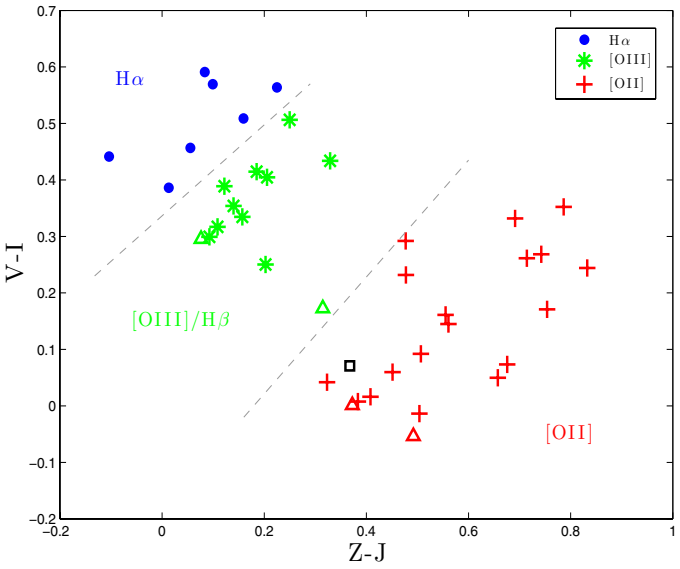

Fig. 6. $Z-J$ versus $V-I$ colour distribution for our basic sample, with V = *F606W*, I = *F814W*, z = *F850LP*, and J = *F125W*, as taken from G13. Solid dots are secure redshifts, open triangles are primary redshift solutions, the black square labels ELG30 for which there is no preferred redshift. As in Bayliss et al. (2011), we see a clear separation of redshifts into separate colour groupings, making this diagram useful as a redshift diagnostic for emission-line-selected samples.

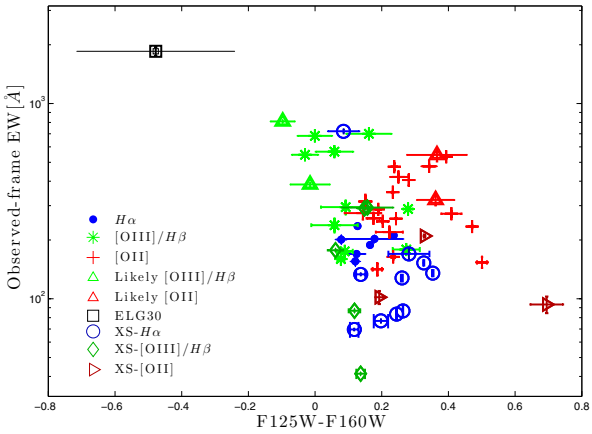

Fig. 7. Observed-frame EW of the line in the NB1060 filter (as derived from the photometry) against (*F125W*−*F160W*) colour for the basic sample and the extended sample (labelled XS in the legend).

We note that ELG30 has the highest equivalent width (EW) emission line of our sample, and that would suggest that it is an [OIII] emitter since they in general have large EW (see e.g. Pénin et al. 2015). Further insight into the redshift of ELG30 comes from Fig. 7, which shows the observed-frame EW of the line in the *NB1060* filter (as derived in Sect. 4.2) against the (*F125W*−*F160W*) colour from the G13 catalogue. For $z = 0.62$ (Hα in *NB1060*), no strong emission lines will be in neither *F125W* nor *F160W*. For $z = 1.12$ ([OIII]5007 in *NB1060*), Hα will be in *F125W* while no strong lines will be in *F160W*. For $z = 1.18$ (Hβ in *NB1060*), no strong lines will be in *F125W* while Hα will be in *F160W*. For $z = 1.85$ ([OII] in *NB1060*), Hβ will be in *F125W* and [OIII]5007 will be in *F160W*. These considerations indicate that a high-EW line emitter with a blue (*F125W*−*F160W*) colour such as ELG30 is more likely to be $z = 1.12$ [OIII]5007 than $z = 1.85$ [OII].

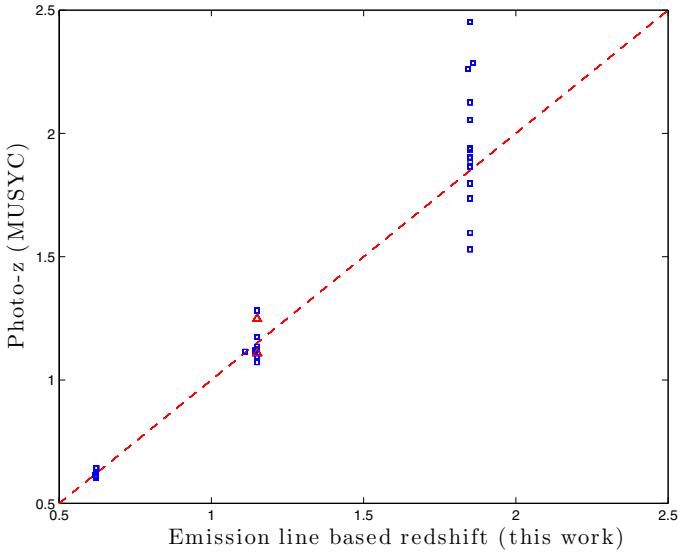

Fig. 8. Redshifts from the MUSYC survey versus redshifts from this work as listed in Table 1. Secure redshift assignments are indicated by blue squares and two "primary redshifts" by red triangles. The agreement with MUSYC redshifts is seen to be good in the mean, but the scatter of the MUSYC redshifts increases at higher redshifts.

All things considered we are not able to assign a primary redshift to ELG30.

3.2.2. Cross-referencing with the MUSYC survey

In Fig. 8 we cross-check our final redshift assignments with those of the MUSYC survey (Cardamone et al. 2010). The MUSYC survey consists of imaging of the GOODS-South field in a wide range of broad and medium-wide filters. The MUSYC catalogue contains photometry for more than 84 000 galaxies including the GOODS field. The catalogue lists magnitudes, photometric and spectroscopic (when available) redshifts, and a wide range of other characteristics. Photometric redshifts have been obtained using the EAZY (Easy and Accurate Zphot from Yale) photometric redshift code (Brammer et al. 2008). In Fig. 8 we plot the MUSYC redshifts against our redshifts, excluding six objects for which we could find no MUSYC counterpart. Two primary redshift assignments (ELG51 and 58) are shown, and the agreement is seen to be good. We therefore conclude that our redshift assignments for those two objects are secure. The last three non-secure redshifts have no counterparts in MUSYC.

It is seen from Fig. 8 that there is very good agreement in the general trend, and the listed errors in the MUSYC catalogue mostly give a reasonable distribution of χ^2, notably for the lower redshift slices. However, four of the 18 certain [OII] emitters are $\approx 2\sigma$ off, one is at 4.6σ, and one at 10.4σ (the latter being ELG12, which has a spectroscopic redshift and is detected in X-rays, and therefore possibly an AGN). We therefore conclude that while the general trend is in excellent agreement and the errors for the $z = 0.62$ slice are very small, the errors become increasingly larger for the two higher redshift slices, and for the $z = 1.85$ slice the errors are underestimated in about 30% of the cases. Therefore galaxy scaling relations derived from large statistical samples based on only photo-z redshifts are probably reliable out to at least $z = 0.6$, but at higher redshifts there are significant, and in some cases significantly underestimated, errors on the redshifts that will propagate into errors on the derived physical parameters, such as stellar masses ($M_\star$) and star

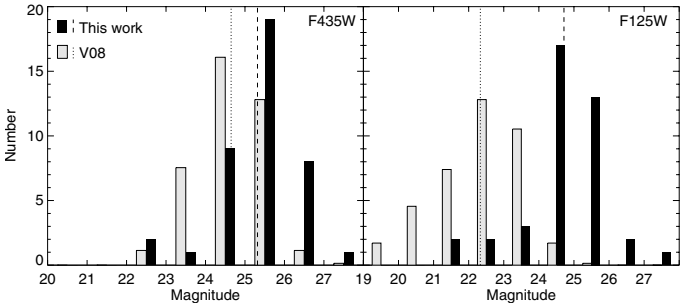

Fig. 9. "De facto" broad-band depth of our basic sample compared to the sample from (Vanzella et al. 2008) (V08), which is one of the deepest existing spectroscopic surveys. The comparison is done in two HST bands corresponding to B (*left panel*) and J (*right panel*). The medians of the samples are shown as dotted and dashed vertical lines. Comparing the medians, our sample is 0.8 and 2.3 mag deeper than V08 in B and J, respectively. The height of the V08 histograms was divided by 7 for easy comparison.

formation rates (SFR). At higher redshifts one might therefore obtain more accurate results from smaller samples but with more accurate redshifts.

3.3. Broad-band flux depth

Our survey function is defined based on the narrow-band flux limit and emission-line equivalent width. This means that we do not have any actual lower limit on broad-band fluxes in our sample. As a result, our survey differs significantly from spectroscopic surveys where strict broad-band flux limits are used for target selection to ensure a good probability that a redshift can be determined from the spectrum. We expect that our sample is deeper than spectroscopic surveys in the same field and to assess how much we have extracted a complete spectroscopic sample from the catalogue of Vanzella et al. (2008) (V08 hereafter). The V08 survey targeted galaxies in the GOODS-S down to a limiting magnitude of z_{850}(AB) = 26, making it one of the deepest existing spectroscopic surveys (cf. Table 5 in Le Fèvre et al. 2015).

From V08 we extracted all objects with redshift in one of our three redshift slices. To obtain a comparison sample of a good size we used slices of width 0.4, centered on the same redshifts, i.e. ±0.2 around $z = 0.62$, 1.15, and 1.85. In Fig. 9 we show the distribution of two broad-band magnitudes ($F435W(\approx B)$ and $F125W(\approx J)$) for both our basic sample (black histogram) and the V08 sample (grey histogram). To make the studies consistent, we obtained the photometry from the G13 catalogue for all objects. It is seen that our sample is significantly deeper in both bands. The median of the comparison sample is 24.71 and 22.56 (B and J, respectively), while our sample has medians 25.49 and 24.92, that is, our sample goes around 0.8 and 2.3 mag deeper.

In the overlapping region between our survey and the recent catalogue of HST grism spectroscopy (Morris et al. 2015), for example, our sample has 33 objects at redshifts probed by the HST spectroscopy ($z > 0.67$), but the HST catalogue contains only the seven brightest of them. The redshifts all agree.

4. Results

4.1. The main sequence of star formation in three narrow redshift slices

The SED fits described in Sect. 3.2 also provide values for $M_\star$ and SFR of each galaxy. We list those values in Table 3, and in Fig. 10 we plot SFR vs. $M_\star$. Both in the local universe and out to a redshift of 3.5, it has been shown that SFR forms a tight correlation with $M_\star$ (Brinchmann et al. 2004; Noeske et al. 2007; Maiolino et al. 2008), the so-called main sequence of star formation (MS). The MS has been shown to evolve with redshift, and in Fig. 10 we have overplotted the relations from the stacked radio data of star-forming galaxies reported in Table 4 of Karim et al. (2011) at each of the redshifts of our three redshift slices. From Karim et al. (2011) we take the mean of their $z = 0.4–0.6$ and $0.6–0.8$ bins to represent $z = 0.62$, their $z = 1.0–1.2$ bin to represent $z = 1.15$, and their $z = 1.6–2.0$

Table 3. Physical parameters resulting from SED fitting with fixed redshift.

ID	log(mass)	log(*SFR*)	Redshift
ELG#	log $M_\odot$	log($M_\odot$/yr)	fixed
3	9.01	0.06	0.619
4	8.63	0.45	1.144
5[c]	9.12	1.41	1.86
6	9.04	1.13	1.86
9	8.15	–0.90	0.62
10	9.27	0.21	0.62
11	7.86	–0.91	0.62
12[c]	10.21	2.38	1.843
14[c]	8.67	0.76	1.85
15[c]	9.12	1.58	1.85
16[c]	9.87	1.52	1.85
20[c]	8.92	1.20	1.85
21[c]	8.89	1.07	1.85
22[c]	9.40	1.84	1.85
23	8.74	0.74	1.85
25[c]	8.86	1.33	1.85
26	8.85	0.36	1.15
28	8.28	–0.37	1.15
34	8.48	–0.63	1.15
35	9.41	1.27	1.85
36	8.31	–0.38	1.15
37	8.49	0.77	1.85
41	8.89	1.02	1.85
43	8.43	–0.29	1.15
45	8.50	–0.55	0.62
51	8.77	0.09	1.15
52	8.43	–0.62	1.15
53	9.61	1.47	1.85
54	9.06	1.53	1.85
55	9.29	1.49	1.15
58	8.68	–0.11	1.15
62	7.97	–1.09	0.62
65	8.61	–0.06	1.15
66[1]	8.48	0.48	1.85
68	9.10	0.61	1.85
70	8.99	0.32	1.15
75[1]	8.50	0.88	1.85
76	9.55	1.56	1.85
78	9.77	1.10	0.624
		Ambiguous cases	
66[2]	7.91	0.38	1.15
75[2]	8.02	0.49	1.15
30[3]	6.72	–1.15	0.62
30[3]	7.31	–0.82	1.15
30[3]	7.83	–0.39	1.85

Notes. [(c)] Cluster member galaxy. [(1)] Primary fixed redshift solution used for ELG66 and 75. [(2)] Secondary fixed redshift solution used for ELG66 and 75. [(3)] No preferred redshift for ELG30, although $z = 0.62$ Hα is disfavoured.

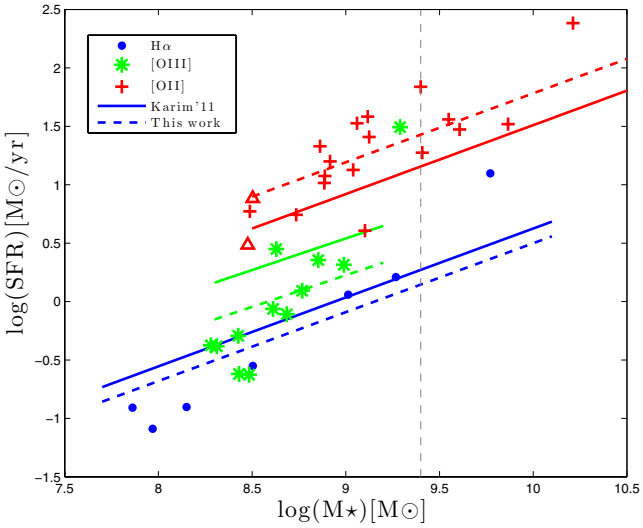

Fig. 10. SFR vs. stellar mass of emission line selected galaxies, color-coded according to their redshift. The two red triangles mark objects with two redshift solutions (only primary solution shown). Solid lines show the relations reported by Karim et al. (2011). Dashed lines are the best fit of relations with the same slopes to our data. The vertical grey dashed line marks the lower mass limit of the Karim et al. (2011) sample.

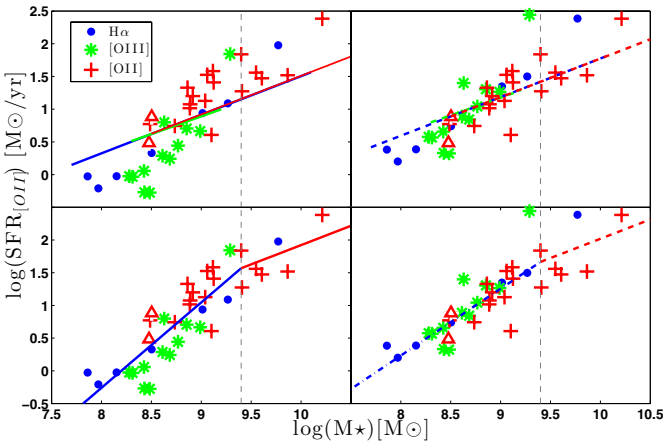

Fig. 11. *Upper two panels*: same data and relations as in Fig. 10. Here we have shifted each redshift slice to remove the effect of redshift evolution. In the *left column* we have applied shifts to bring the blue and green solid lines on top of the red (i.e. applied redshift corrections as reported in Karim et al. 2011), in the right we did the same but used the dashed lines. *Lower panels*: best fit of broken MS relations. It is seen that under both assumptions, the relation steepens towards lower stellar masses.

Table 4. Offsets of SFR($M_\star$) relative to Karim et al. (2011).

z	$N_{\rm obj}$	*SFR* offset	rms
0.62	7	-0.13 ± 0.16	0.35
1.15	12[1]	-0.33 ± 0.13	0.43
1.15	14[2]	-0.22 ± 0.16	0.52
1.85	19[1]	0.26 ± 0.07	0.27
1.85	17[2]	0.29 ± 0.07	0.27
All	38[1]	0.33 ± 0.05	0.32
All	38[2]	0.35 ± 0.06	0.34

Notes. The first 5 lines report the offset of individual redshift subsamples assuming for each the slope found by Karim et al. (2011). The last two are best fit offset of the entire sample assuming now a slope of 1.17 for the galaxies with mass below the mass completeness limit ($10^{9.4}$ $M_\odot$) of the Karim et al. (2011) sample. In both cases we repeat the fit using secondary redshifts for ELG 66 and 75 but no significant change is seen. [(1)] Primary redshift solution used for ELG 66 and 75. [(2)] Secondary redshift solution used for ELG 66 and 75.

bin to represent $z = 1.85$. Both the data and the relations are colour-coded according to a redshift slice as in Fig. 6. We also plot $\log(M_\star) = 9.4$ which is the lower limit of the samples considered by Karim et al. (2011). One object (ELG14) turned out to provide unstable physical parameters in the sense that leaving out a single photometric point would severely change the output parameters. Upon checking the HST image, we noted a close neighbour galaxy of different colour, which presumably could have affected the photometry and caused this. The redshift is good so we keep it in the sample, but we exclude it from the analysis of the MS relation. We also exclude ELG30 from this analysis since we do not have a redshift for it. We use the primary redshift solutions for ELG66 and 75, but repeat the analysis using the secondary solutions. No significant difference is found using the secondary solutions (see Table 4).

From Fig. 10 we see that our data roughly agree with the relation from Karim et al. (2011), i.e. that there is a MS and that it evolves with redshift in the sense that galaxies of a given stellar mass have lower SFR at lower redshifts. Our data points are somewhat offset from the expected relations, but this could possibly be because our objects sample a much lower stellar mass range than the relations we compare them to. If the MS, for example, is steepening at the low-mass end, it would cause our low-mass galaxies to drop below the relations. To test this, we first assume that the slopes reported by Karim et al. (2011) at each of our redshift slices are correct for all masses, and then we determine the offsets to our data. The best fit offsets are shown as dashed coloured lines in Fig. 10 and provided in Table 4. We then remove the effect of redshift evolution in two different ways. First we assume that the evolution from Karim et al. (2011) is correct, and we apply a shift that brings all galaxies (and the relations) to what they would have been in the [OII] redshift slice (upper left panel of Fig. 11). We then fit a broken linear relation to the data points with the following two conditions: (i) at $\log(M_\star)$ larger than 9.4 it must have the slope of 0.59 (from Karim et al. 2011) and (ii) it must be continuous in $\log(M_\star) = 9.4$. The resulting best fit is shown in lower the left-hand panel of Fig. 11, and the best fit slope is found to be 1.31 with an rms of 0.31. In the two right-hand panels of Fig. 11, we show the same as in the left, only here we have applied redshift correction shifts so that the dashed lines in Fig. 10 are lined up rather than the solid lines. In this case the best fit gives a slope of 1.02 with an rms of 0.29.

Our sample reaches stellar masses 1.5 decades lower than the sample of Karim et al. (2011), and we see that in the range below their lower mass limit, our sample follows a significantly steeper MS, no matter how we correct for the redshift evolution. Previous analyses of the derived stellar masses from SED fits with exponential declining and increasing star-formation rates in a population of star-forming galaxies at $z = 1$–2 have shown that the stellar masses vary within ~0.1 dex (Christensen et al. 2012). As noted above, the offsets we reported in Table 4 may in this case be dominated by this steepening of the slope, and we therefore repeat the fit using a more realistic assumption. Rather than assuming a constant slope, we now use a slope with a break at $\log(M_\star) = 9.4$. For the high-mass end we use the slope of 0.59

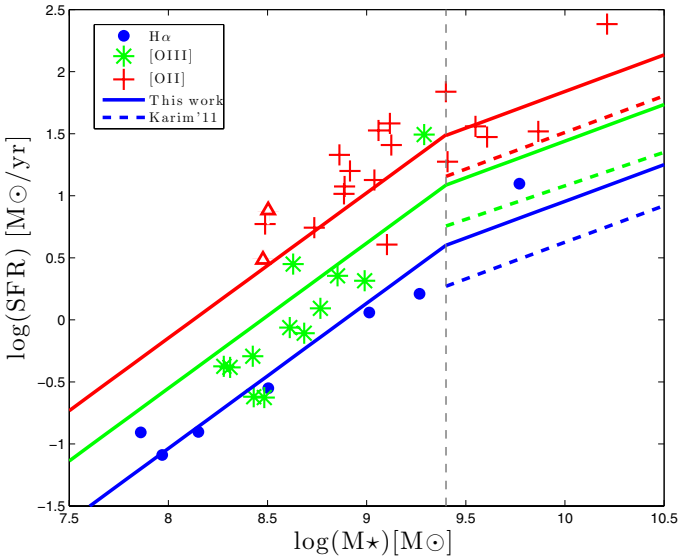

Fig. 12. Similar to Fig. 10. Here we show only the Karim et al. (2011) fits (dashed lines) in the range above their lower mass bound. The full lines now show the best fit to our data of a "broken" MS with a steeper low mass slope.

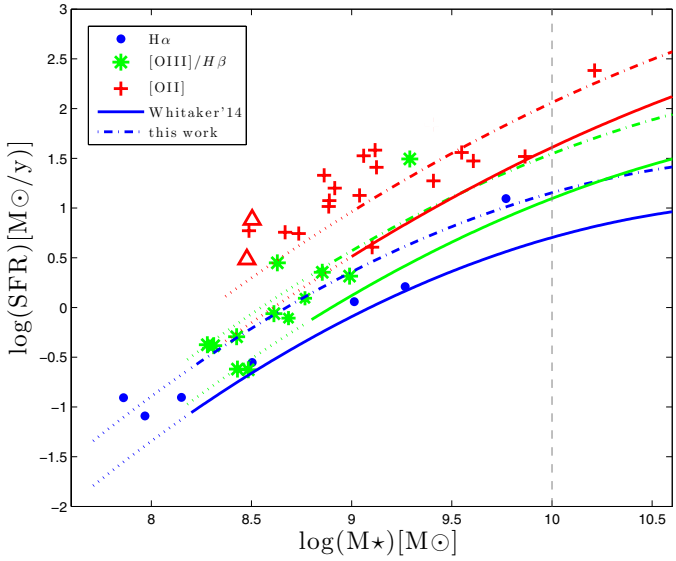

Fig. 13. Similar to Fig. 12. Here we compare to the study by Whitaker et al. (2014) (solid lines), who also report a steepening towards low stellar masses. Their SFRs are seen to be lower, but adding 0.45 to their fits, we obtain a better fit to our data (dash-dotted curves). We do not see any evidence for shallower redshift evolution at low masses as they report. The dashed vertical line marks the division between their individual object (above 10^{10}) and stacked object (below 10^{10}) fits. Dotted curves are extrapolations of their fits where they had no data.

from Karim et al. (2011), and for the low-mass end we use the mean of the slopes we found above, which is 1.17.

The resulting best fit is shown in Fig. 12 and again reported in Table 4. We see that allowing for the change of slope, we now get a consistent positive offset towards higher SFR in all three redshift slices. This is no great surprise because one would expect samples selected by narrow-band techniques to select the objects with the strongest emission lines in any stellar mass bin, and consequently to contain the highest SFR galaxies of any mass at any redshift. In that sense our sample defines the upper envelope of the MS for low-to-intermediate-mass galaxies.

In conclusion to this section, we first tested that our sample was offset (up or down) in SFR compared to Karim et al. (2011) using their reported slope. We found an inconsistent scatter with both positive and negative offsets, but this could be because the median $M_\star$ is different in the three redshift slices. We then removed the effect of redshift to make them easier to compare and noted evidence that the slope is steeper at low masses. Assuming a steeper slope in the low-mass end we find that our data are consistent with a constant offset from the Karim et al. (2011) data (at 6.6σ) with an internal scatter of 0.32. Performing the same fit to the data, but instead using the constant slope of Karim et al. (2011) at all masses gives a zero offset with an internal scatter of 0.43, which is a significantly poorer fit even allowing for the one degree of freedom less.

Comparison with other studies

Whitaker et al. (2014) present MS fits from a study of galaxies in the CANDELS fields. At stellar masses larger than $\sim 10^{10}\ M_\odot$ they use a UV+IR SFR indicator on photometry of individual photo-z galaxies, at lower stellar masses they do the same on stacked photometry and reach stellar masses of $10^{8.4}$ (at $z = 0.5$) to $10^{9.2}$ (at $z = 2.5$). Similar to our results of the previous section, they report a steepening of the slope at lower masses, but they fit it with a polynomial rather than a broken power law. They also report a shallower redshift evolution of the MS at lower masses than at high masses. Lee et al. (2015) also report a steepening of the MS below $M_* = 10^{10}\ M_\odot$, in agreement with our results.

We interpolated the polynomial fits of Whitaker et al. (2014) (their Eq. (2)) to our three redshift slices and plot them with our data in Fig. 13. It is seen that the steepening is in good agreement with what we have reported, but the normalization is again lower than our data. Also in Fig. 13 we show the Whitaker et al. (2014) models where we have added 0.45 to the log(SFR), which provide a better fit to our data, but it is seen that they find much less redshift evolution than seen in our sample. In particular we do not see any evidence of less evolutuion of the MS at low stellar masses, and our sample appears in stark disagreement with that result. We note, however, that our data are from SED fits to individual galaxies, while Whitaker et al. (2014) were fitting theirs to stacked data in the regime of comparison. Nilsson et al. (2011) performed a test fitting 40 emission-line-selected galaxies both individually and as a stack, and concluded that "Stacking of objects does not reveal the average of the properties of the individual objects". The difference could therefore be related to the stacking.

4.2. SFRs from SED fitting and from emission lines

From the NB magnitude we can calculate the emission-line fluxes since the flux density in the narrow band is equal to the sum of the emission line flux density and the continuum flux density: $f_{\nu,\mathrm{NB}} = f_{\nu,\mathrm{line}} + f_{\nu,\mathrm{cont}}$. For each galaxy, we derive the underlying continuum flux density from the best fit SED model by interpolating the flux density in adjacent 50 Å intervals blue and redwards of the NB filter. The continuum flux density is subtracted from the NB flux density taking the NB transmission curve into account. The derived emission line fluxes and equivalent widths (EWs) in the observed frame are listed in Table 1. The results are consistent if we choose to derive the continuum flux density by interpolating between the observed magnitudes

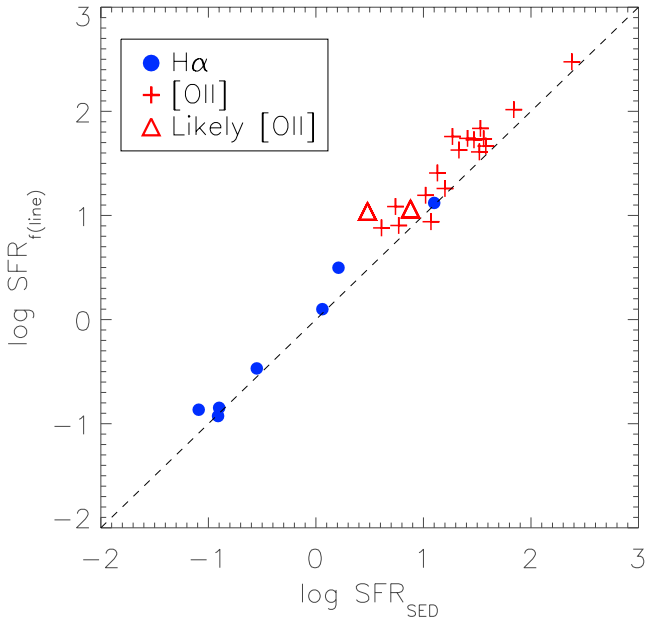

Fig. 14. SFRs derived from the emission line flux plotted against the SFR values obtained from the SED fitting method. Symbol shapes and colours are similar to those in Fig. 10. The two methods show the offset of 0.19 ± 0.05 dex, which means that the values derived with two different methods are in excellent agreement for the entire sample.

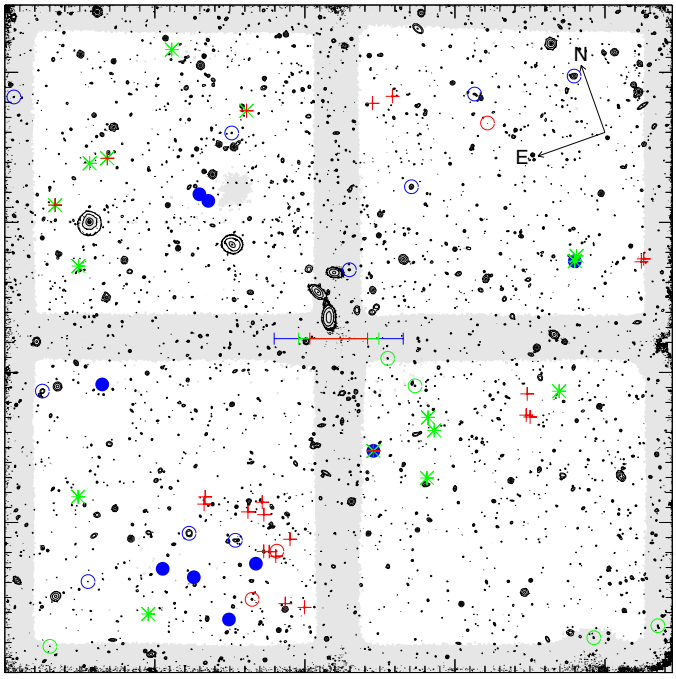

Fig. 15. Objects identified in the three redshift slices overplotted on the narrow-band image (black contours). Blue dots are Hα emitters, green asterisks are [OIII]/Hβ, and red crosses represent the [OII] emitters. Lower S/N areas of the image that were excluded from the basic sample are shaded in grey. Multiple symbols that are over-plotted represent galaxies with multiple redshift solutions. Open circles represent galaxies from the "extended sample". Bars of length 1 comoving Mpc at the given redshift is over-plotted in the centre of the image with same colour-coding as for the objects.

in the ACS/*F850LP* and WFC3/*F125W* bands and assuming a power-law spectral slope between the bands.

For ELG 30, where we do not have a preferred redshift, the line flux for $z = 0.62, 1.15, 1.85$ is $3.17 \pm 0.16, 2.96 \pm 0.16, 2.97 \pm 0.16 \times 10^{-17}$ erg/s/cm^2, and the EWs are 2011.4 ± 106.4, 1851.6 ± 97.9, 1969.8 ± 104.2 Å. In Table 1 we list the value for $z = 1.15$.

Emission lines provide us with an alternative for measuring the SFR. We correct the emission line fluxes for intrinsic reddening using the best fit $E(B-V)$ from the LePhare fits and a Calzetti extinction curve. We then calculate Hα and [OII] luminosities, which are converted to a SFR using the calibrations in Kennicutt (1998), and we include a downward correction of a factor of 1.8 to correct from a Salpeter to a Chabrier IMF. The result is shown in Fig. 14, which demonstrates that there is excellent agreement between the SFRs derived from emission lines and from the SED fits. In fact the average offset in the SFR is just 0.19 ± 0.05 dex between the two different methods. Assuming a typical [NII]/Hα ratio of 0.1 appropriate for low-mass galaxies, the emission line fluxes and the blue points in Fig. 14 will have a downward correction of 0.05 dex. By Including this correction, the offset between the emission line derived SFRs and the SED SFRs is 0.17 ± 0.05.

4.3. Clustering and large scale structure in three narrow redshift slices

In this section we consider the extended sample of 58 objects in three redshift slices. In Fig. 15 we plot the objects in the three redshift slices overlaid on our narrow-band image (in black contours). In this figure we also show the masked lower signal-to-noise regions (shaded grey). The same field covers different physical scales and different comoving scales in the three redshift slices. In Fig. 16 we again plot the three slices separately, but here we have scaled them all to the same comoving scale. We subsequently found that the $z = 1.84$ cluster has been discovered independently in a study based on CANDELS and 3D-HST spectroscopic redshifts in the field (Mei et al. 2015). We refer the reader to this work for further discussion of this interesting structure.

One feature that is immediately visible is the concentration of [OII] emitters in the lower left-hand quadrant. In Sect. 4.1 we found that the [OII] emitter sample on average has higher mass than galaxies in the other slices, so because high-mass galaxies are known to cluster more strongly than low-mass galaxies, this is indeed the slice where we would be most likely to find a galaxy cluster. In Fig. 16 we have drawn a circle with a diameter of 2.55 comoving Mpc, which encloses 13 of the 23 [OII] emitters in our extended sample. We also labelled the position of the highest mass galaxy in our sample, and it is seen to fall very close to the centre of the circle. From Fig. 15 we see that there is indeed evidence of higher density of both optical and X-ray sources (Xue et al. 2012) around the position of the clump of [OII] emitters. Computing the surface density of galaxies inside the circle, we find 2.5 per comoving Mpc^2, while outside of that it is 0.08 per comoving Mpc^2. On the basis of the observations reported above, we here conclude that we have identified a galaxy cluster at $z = 1.85$ in our [OII] redshift slice.

Simulations of early galaxy and structure formation all share a common prediction that the first structures to form are filaments whose ends are connected in nodes. Young low-mass galaxies form in the filaments, and while they assemble further and grow, they also drift along the filaments into the nodes where they form galaxy groups and eventually clusters (Monaco et al. 2005). Samples of high-mass galaxies are therefore strongly clustered and well suited to identifying the nodes as we showed in the previous paragraph, but to identify filaments one needs

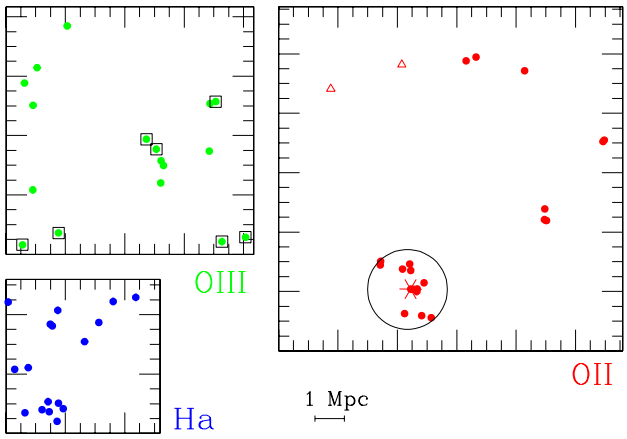

Fig. 16. Objects detected in the three redshift slices shown separately and scaled to the same co-moving scale. The colour coding is as in previous figures: dots denote certain redshifts from the extended sample, and open triangles indicate primary redshifts for the two uncertain cases. Open black squares indicate objects with known spectroscopic redshifts in the [OIII] slice. The red star in the [OII] slice marks the galaxy with the highest $M_\star$, and the large black circle the cluster centered on it at $z = 1.85$.

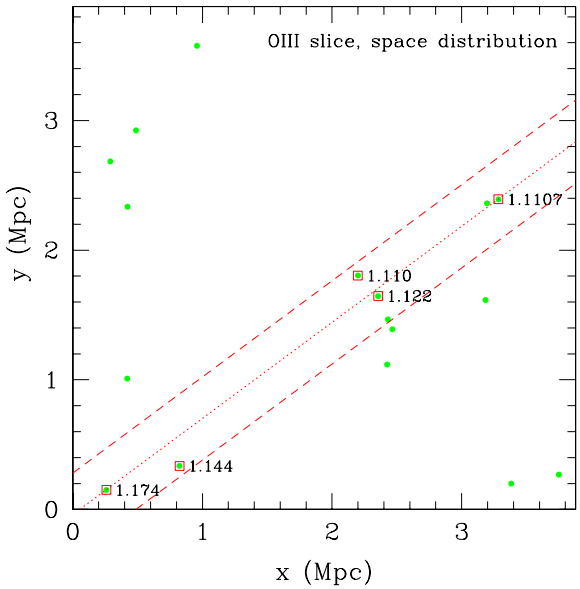

Fig. 17. Objects detected in the [OIII] slice but now at proper scale. The red dotted and dashed lines provide the size scale of the filament of emission line galaxies at $z = 3.04$ reported by Møller & Fynbo (2001). Also we show the spectroscopic redshifts of five galaxies that may outline a similar filament at $z = 1.15$ in this field.

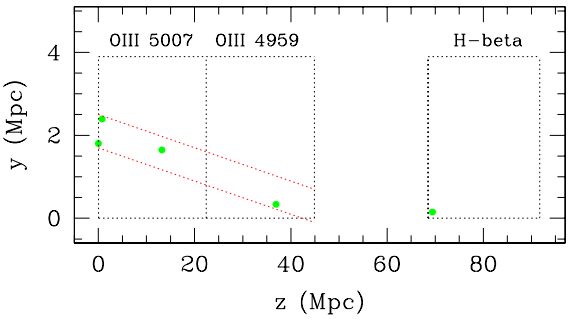

Fig. 18. Similar to Fig. 17 but with converted redshifts to proper distance. We show the projection onto the (y vs. distance) plane. For comparison we again indicate a filament of the same proper width as in Fig. 17. The [OIII] slice covers a z-range about four times wider than the other slices because of the three emission lines. Selection by each of the three lines is indicated by the dotted lines.

samples of lower mass galaxies covering volumes large enough to cover the expected sizes of filaments (20–25 h^{-1} Mpc), (Demiański & Doroshkevich 1999). The end product of the evolution of this cosmic web has been well studied at low redshift, and recently a large catalogue of filaments in the redshift range $z = 0.009-0.155$ has been published Tempel et al. (2014), but at higher redshifts than 0.155 this becomes much very difficult. Warren & Møller (1996) argued that Lyα emission-line-selected galaxies have lower masses than continuum-flux-selected samples, and suggested that they could be used to identify filaments. Møller & Warren (1998) showed on a statistical basis that Lyα emitters do tend to line up in strings. Nevertheless, the actual mapping of filaments is hampered by two problems: mostly the observed volumes are too small, and there is usually no follow-up spectroscopy, which is required to provide the 3D mapping of the volume.

In one case a fully resolved filament mapped in Lyα was identified at $z = 3.04$ (Møller & Fynbo 2001) where a total of eight objects were found to be enclosed in a cylinder with proper radius 400 kpc which in the cosmology we use here also corresponds to 400 kpc. In Fig. 16 we see that 10 out of 17 galaxies at $z = 1.15$ lie close to a line going almost diagonally from the lower left-hand corner of the field towards the upper right. This could be a chance alignment of galaxies at mixed redshifts, but it could also be a filament seen under some inclination angle. As in the work by Møller & Fynbo (2001) our field is too small to identify a filament that lies in the plane of the sky, we would see too few objects in such a small filament section. To test that we do indeed have enough 3D information, we also in Fig. 16 indicated those objects in the [OIII] slice for which we have spectroscopic redshifts, and we see that we have five spectroscopic redshifts covering the entire length of the diagonal.

In Fig. 17 we again plot the objects in the [OIII] slice, but here on proper length scale and with the redshifts of the five galaxies on the diagonal line marked. We see that the redshifts in general grow from the upper right towards the lower left, so this does indeed appear to be a filament pointing from the upper right towards the lower left away from us. To compare this to the previously reported Lyα filament, we have indicated the width (400 kpc) of that filament on top of this one, and all five objects are seen to fit well within this cylinder in this projection. The availability of spectroscopic redshifts allows us to also compute the arrangement of the objects along the line of sight.

The [OIII] redshift slice is thicker than the other two slices because we have three individual lines ([OIII] 5007, [OIII] 4959, and Hβ) here, either of which could fall into the narrow pass band. We visualize this in Fig. 18 where we have kept the field y-axis of Fig. 17, but have turned the volume 90 degrees and replaced the x-axis by the z-axis (i.e. redshift converted to proper distance). The three dotted boxes here represent the volumes sampled by each of the three emission lines, green dots are the galaxies, and the diagonal dashed lines again mark out a filament of thickness as in Fig. 17. We see that the first four galaxies would indeed fit into a straight, cylindrical filament of this thickness, but it would be somewhat longer than the Lyα filament at redshift 3.04. The last galaxy seen in Hβ may well belong to the same filament, but it would have to be bent or thicker in that case. The length of the filament is in excellent agreement with the detection of the Lyα filament at $z = 3.01$ reported by Matsuda et al. (2005) and the recent work at low redshifts Tempel et al. (2014).

In conclusion, we have shown that emission line selected galaxies at those redshifts are well suited to performing observational tests of simulations of a large scale structure. The Hα field size is in this case too small, but surveys over larger fields like UltraVISTA (McCracken et al. 2012; Milvang-Jensen et al. 2013) will provide fields of sufficient size. The [OII] slice has a larger volume, and in general the [OII] selected galaxies have higher mass than the lower redshift slices, making the [OII] slice ideal for rich group and cluster statistics. The [OIII] slice is extremely well suited for filament searches because the depth allows to identify filaments at any inclination angle. This promises that it may soon be possible to perform the alternative and "purely geometrical" cosmological test and determine Ω_Λ using filaments as described in detail by Weidinger et al. (2002). Identifying filaments require spectroscopic redshifts, or some other diagnostic for more accurate redshift determination. One such novel method using only VISTA narrow-band data has recently been described (Zabl et al., in prep.).

5. Discussion and conclusions

5.1. Galaxy scaling relations at low masses

Understanding the scaling relations of galaxies of all masses is fundamental to understanding galaxy formation and evolution. Nevertheless, galaxy samples selected in all emission bands ranging from X-rays, through UV, optical, IR, sub-mm, and mm, to radio, all form flux-limited samples of galaxies that are the most luminous, and presumably the most massive, of their kind. Such samples are, by definiton, the easiest to obtain, and normally large portions of our knowledge of high-redshift galaxies come from such samples. However, to explore the low-mass range of galaxies, notably at high redshifts, other selection techniques are required. One such technique is emission line selection via deep narrow and broad band imaging.

We are involved in several narrow/broad band imaging surveys, and in this paper we reported on a pilot project to study the feasibility of using them to trace low-mass galaxy scaling relations and their redshift evolution. Simple narrow/broad emission line selection allows galaxies to be selected with strong emission lines, thereby providing a deepening of the flux-limited samples, and here we have specifically chosen a broad-narrow-broad selection that results in a selection of the highest emission-line equivalent width galaxies. Two simple predictions for a study of this kind would be:

(*i*) that our sample in the mean could have higher SFR for any given galaxy stellar mass; and
(*ii*) that our sample in the mean will select galaxies down to lower stellar masses than continuum flux-limited samples.

We carried out a detailed comparison of our dataset to previous studies and find that both of those predictions have been confirmed. We thus provide an "upper boundary" to the main sequence of star formation (MS) at each of the three redshifts we studied.

Our comparison to previous work also shows that the MS has a significantly steeper slope at the low-mass end (below $M_\star = 10^{9.4}$) than at higher masses.

5.2. Narrow-band selection as cosmological tool

Any narrow/broad band survey carried out at a wavelength in excess of the rest wavelength of Hα provides a roughly even coverage of three widely separated narrow redshift slices corresponding to the redshifted wavelengths of Hα, [oIII]/Hβ, and [oII]. A few additional species at other wavelengths will also appear on occasion, but only rarely, owing to the much weaker strength of their transitions. The exact ratio of detected objects between the three main slices depends on their relative equivalent widths (as a function of redshift), their relative number density (as a function of redshift), and the ratio of the surveyed volumes (as a function of narrow-band wavelength and assumed cosmology).

We surveyed comoving volumes of 1221 Mpc^3 (Hα), 3092 Mpc^3 ($\times$3 due to Hβ, [OIII]λ4959, and [OIII]λ5007), and 5536 Mpc^3 ([OII]). Down to our conservatively chosen narrow-band AB magnitude limit of 24.8, they are distributed in the following proportions: Hα emitters 20%, [OIII]/Hβ emitters 30%, and [OII]-emitters 50% (see Fig. 5). We compared our redshifts to previous photo-z redshifts from the literature and showed that narrow-band selection allows a much more accurate redshift assignment, notably in the highest redshift slices. The errors on redshift assignment from photo-z will propagate into errors on the physical parameters ($M_\star$ and SFR), so that smaller, but more accurate, samples of narrow-band-selected galaxies will provide checks of whether the propagated errors simply add scatter or if they add systematic effects.

We showed that the galaxies can be classified fairly robustly based on two broad-band colours (Fig. 6), confirming the earlier study by Bayliss et al. (2011). Therefore, we conclude that emission-line selected galaxies do indeed split into the evolutionary groups according to their colour. In Fig. 10 we see that the galaxies in our lowest redshift slice have on average the lowest masses and that galaxies then become progressively more massive at higher redshifts. This could possibly be related to the selection via different emission lines in the three slices, but is more likely a result of using the same observed magnitude limit for all slices. One very interesting thing to note is that we are able to select star-forming galaxies of stellar masses down to $10^{8.5}$ $M_\odot$ at a redshift of 1.85, and well below the masses in the other two slices. With emission-selected samples, it is very difficult to study low-mass galaxies beyond the critical redshift of "cosmic high noon" at $z = 2.5$, but absorption-selected galaxy samples and samples selected as gamma ray burst host galaxies (GRBs) have been shown to reach much lower masses (Møller et al. 2013; Christensen et al. 2014; Arabsalmani et al. 2015). Therefore, to be able to connect absorption and GRB-selected samples (with median $M_\star$ of $10^{8.5}$ $M_\odot$) with continuum-emission-selected samples at high redshifts, it is important to create well-studied samples with a wide overlap in stellar masses. Absorption-selected galaxies are in general more easily identified via line emission than via continuums emission (e.g. Weatherley et al. 2005; Rauch et al. 2008; Fynbo et al. 2010, 2011, 2013), and the ongoing UltraVISTA (McCracken et al. 2012) narrow-band survey covering $\approx$0.8 deg^2 at slightly higher redshifts (for Hα: $z = 0.815$, for [OIII]/Hβ: $z = 1.38/1.45$ and for [OII]: $z = 2.19$) will create a large sample of low-mass emission-line-selected galaxies in those three slices (Milvang-Jensen et al. 2013). The UltraVISTA sample will be well suited to connecting the current flux-limited galaxy samples out to the highest redshifts ($z = 6-8$) currently explored by DLA galaxies and GRBs.

One of the objectives of this paper was to derive more robust forecasts of what will be found in ongoing or upcoming deep surveys, in particular the UltraVISTA survey (McCracken et al. 2012; Milvang-Jensen et al. 2013). The UltraVISTA survey uses a slightly redder narrow-band filter centred at 1.19 μm (Milvang-Jensen et al. 2013), but this difference is small enough that evolutionary effects on the population of $z < 2$ emitters (Hα, [oIII]/Hβ and [oII]) should be small. We can thus make forecasts

of which numbers of the most common types of such emitters we expect to find in the UltraVISTA survey based on the present work. After scaling with the area, we expect to detect $\gtrsim$1000 of each of the Hα, [OIII], and [OII] emitters. Given the large area of the UltraVISTA we predict that we will find more rare line emitters that are not represented in the more than 70 times smaller area sampled in the present work.

5.3. Structure formation traced by emission-line-selected galaxies

In Fig. 12 we show that objects in the [OII] slice on average have higher masses than in the other two slices. As argued by Møller & Fynbo (2001) and Monaco et al. (2005), the lowest mass galaxies at any redshift are the best candidates for mapping out the filamentary structure of the cosmic web, while the higher mass galaxies will be more clustered around the nodes of the web and could thus mark the sites of early cluster formation.

In this paper we have pursued their line of thought and identified a galaxy cluster (or proto cluster) at $z = 1.85$. The cluster has an elliptical shape as predicted by N-body simulations and has no extended X-ray emission, so it is probably in its early stages of formation. The galaxy with the highest mass of our entire sample lies in the centre of the forming cluster and has been identified as an X-ray emitter. This makes this galaxy especially interest since it is a very good candidate for the pre-stage of a central cluster cD galaxy.

Secure identification of filaments is more difficult since it requires even better redshift determinations than the narrow-band data alone can provide. We identified a possible filament that lies diagonally across the field of the [OIII] slice, and enough of the objects had known spectroscopic redshifts for a 3D mapping. The candidate filament has width and length in good agreement with simulations and with the previous detection of Møller & Fynbo (2001). Obtaining a few more redshifts would be good in order to securely confirm the identification, but detecting a forming cluster and a likely filament are examples of the strong potential of tracing the formation of structure in the early universe with deep narrow-band data.

Acknowledgements. We thank Thomas Krühler and Jens Hjorth for useful suggestions. Special thanks to Olivier Ilbert for immense help with the LePhare code. We thank the referee for comments that helped improve the paper. The Dark Cosmology Centre is funded by the DNRF. The research leading to these results has received funding from the European Research Council under the European Union's Seventh Framework Programme (FP7/2007−2013)/ERC Grant agreement no. EGGS-278202. B.C. acknowledges support from the ERC starting grant CALENDS. This research has made use of the SIMBAD database, operated at the CDS, Strasbourg, France.

References

Arabsalmani, M., Møller, P., Fynbo, J. P. U., et al. 2015, MNRAS, 446, 990
Arnouts, S., Cristiani, S., Moscardini, L., et al. 1999, MNRAS, 310, 540
Balestra, I., Mainieri, V., Popesso, P., et al. 2010, A&A, 512, A12
Bayliss, K. D., McMahon, R. G., Venemans, B. P., Ryan-Weber, E. V., & Lewis, J. R. 2011, MNRAS, 413, 2883
Brammer, G. B., van Dokkum, P. G., & Coppi, P. 2008, ApJ, 686, 1503
Brinchmann, J., Charlot, S., White, S. D. M., et al. 2004, MNRAS, 351, 1151
Bruzual, G., & Charlot, S. 2003, MNRAS, 344, 1000
Calzetti, D., Armus, L., Bohlin, R. C., et al. 2000, ApJ, 533, 682
Cardamone, C. N., van Dokkum, P. G., Urry, C. M., et al. 2010, ApJS, 189, 270
Castellano, M., Fontana, A., Boutsia, K., et al. 2010, A&A, 511, A20
Castro Cerón, J. M., Michałowski, M. J., Hjorth, J., et al. 2010, ApJ, 721, 1919
Chabrier, G. 2003, PASP, 115, 763
Christensen, L., Hjorth, J., & Gorosabel, J. 2004, A&A, 425, 913
Christensen, L., Richard, J., Hjorth, J., et al. 2012, MNRAS, 427, 1953
Christensen, L., Møller, P., Fynbo, J. P. U., & Zafar, T. 2014, MNRAS, 445, 225
Clément, B., Cuby, J.-G., Courbin, F., et al. 2012, A&A, 538, A66
Daddi, E., Dickinson, M., Morrison, G., et al. 2007, ApJ, 670, 156
Demiański, M., & Doroshkevich, A. G. 1999, MNRAS, 306, 779
Fynbo, J. P. U., Ledoux, C., Møller, P., Thomsen, B., & Burud, I. 2003, A&A, 407, 147
Fynbo, J. P. U., Laursen, P., Ledoux, C., et al. 2010, MNRAS, 408, 2128 (F10)
Fynbo, J. P. U., Ledoux, C., Noterdaeme, P., et al. 2011, MNRAS, 413, 2481
Fynbo, J. P. U., Geier, S. J., Christensen, L., et al. 2013, MNRAS, 436, 361
Giavalisco, M., Ferguson, H. C., Koekemoer, A. M., et al. 2004, ApJ, 600, L93
Goldoni, P. 2011, Astron. Nachr., 332, 227
Guo, Y., Giavalisco, M., Ferguson, H. C., Cassata, P., & Koekemoer, A. M. 2012, ApJ, 757, 120
Guo, Y., Ferguson, H. C., Giavalisco, M., et al. 2013, ApJS, 207, 24
Hodge, J. A., Karim, A., Smail, I., et al. 2013, ApJ, 768, 91
Ilbert, O., Arnouts, S., McCracken, H. J., et al. 2006, A&A, 457, 841
Jacobs, B. A., Sanders, D. B., Rupke, D. S. N., et al. 2011, AJ, 141, 110
Karim, A., Schinnerer, E., Martínez-Sansigre, A., et al. 2011, ApJ, 730, 61
Kennicutt, Jr., R. C. 1998, ARA&A, 36, 189
Koyama, Y., Smail, I., Kurk, J., et al. 2013, MNRAS, 434, 423
Krühler, T., Greiner, J., Schady, P., et al. 2011, A&A, 534, A108
Le Fèvre, O., Vettolani, G., Paltani, S., et al. 2004, A&A, 428, 1043
Le Fèvre, O., Tasca, L. A. M., Cassata, P., et al. 2015, A&A, 576, A79
Le Floc'h, E., Duc, P.-A., Mirabel, I. F., et al. 2003, A&A, 400, 499
Ledoux, C., Petitjean, P., Fynbo, J. P. U., Møller, P., & Srianand, R. 2006, A&A, 457, 71
Lee, N., Sanders, D. B., Casey, C. M., et al. 2015, ApJ, 801, 80
Ly, C., Malkan, M. A., Kashikawa, N., et al. 2012, ApJ, 757, 63
Maiolino, R., Nagao, T., Grazian, A., et al. 2008, A&A, 488, 463
Malhotra, S., & Rhoads, J. E. 2004, ApJ, 617, L5
Matsuda, Y., Yamada, T., Hayashino, T., et al. 2005, ApJ, 634, L125
McCracken, H. J., Milvang-Jensen, B., Dunlop, J., et al. 2012, A&A, 544, A156
Mei, S., Scarlata, C., Pentericci, L., et al. 2015, ApJ, 804, 117
Michałowski, M., Hjorth, J., & Watson, D. 2010, A&A, 514, A67
Mignoli, M., Cimatti, A., Zamorani, G., et al. 2005, A&A, 437, 883
Milvang-Jensen, B., Freudling, W., Zabl, J., et al. 2013, A&A, 560, A94
Møller, P., & Fynbo, J. U. 2001, A&A, 372, L57
Møller, P., & Warren, S. J. 1993, A&A, 270, 43
Møller, P., & Warren, S. J. 1998, MNRAS, 299, 661
Møller, P., Fynbo, J. P. U., Ledoux, C., & Nilsson, K. K. 2013, MNRAS, 430, 2680
Monaco, P., Møller, P., Fynbo, J. P. U., et al. 2005, A&A, 440, 799
Morris, A. M., Kocevski, D. D., Trump, J. R., et al. 2015, ApJ, 149, 178
Nilsson, K. K., Orsi, A., Lacey, C. G., Baugh, C. M., & Thommes, E. 2007, A&A, 474, 385
Nilsson, K. K., Östlin, G., Møller, P., et al. 2011, A&A, 529, A9
Noeske, K. G., Weiner, B. J., Faber, S. M., et al. 2007, ApJ, 660, L43
Partridge, R. B., & Peebles, P. J. E. 1967, ApJ, 147, 868
Pénin, A., Cuby, J.-G., Clément, B., et al. 2015, A&A, 577, A74
Pritchet, C. J., & Hartwick, F. D. A. 1987, ApJ, 320, 464
Rauch, M., Haehnelt, M., Bunker, A., et al. 2008, ApJ, 681, 856
Ravikumar, C. D., Puech, M., Flores, H., et al. 2007, A&A, 465, 1099
Rodrigues, M., Hammer, F., Flores, H., et al. 2008, A&A, 492, 371
Shapley, A. E. 2011, ARA&A, 49, 525
Sobral, D., Best, P. N., Smail, I., et al. 2014, MNRAS, 437, 3516
Steidel, C. C., Adelberger, K. L., Shapley, A. E., et al. 2003, ApJ, 592, 728
Straughn, A. N., Kuntschner, H., Kümmel, M., et al. 2011, AJ, 141, 14
Szokoly, G. P., Bergeron, J., Hasinger, G., et al. 2004, ApJS, 155, 271
Tempel, E., Stoica, R. S., Martínez, V. J., et al. 2014, MNRAS, 438, 3465
Trump, J. R., Weiner, B. J., Scarlata, C., et al. 2011, ApJ, 743, 144
Vanzella, E., Cristiani, S., Dickinson, M., et al. 2005, A&A, 434, 53
Vanzella, E., Cristiani, S., Dickinson, M., et al. 2006, A&A, 454, 423
Vanzella, E., Cristiani, S., Dickinson, M., et al. 2008, A&A, 478, 83
Vernet, J., Dekker, H., D'Odorico, S., et al. 2011, A&A, 536, A105
Villforth, C., Sarajedini, V., & Koekemoer, A. 2012, MNRAS, 426, 360
Warren, S. J., & Møller, P. 1996, A&A, 311, 25
Weatherley, S. J., Warren, S. J., Møller, P., et al. 2005, MNRAS, 358, 985
Weidinger, M., Møller, P., Fynbo, J. P. U., Thomsen, B., & Egholm, M. P. 2002, A&A, 391, 13
Wenger, M., Oberto, A., Bonnarel, F., et al. 2007, in Library and Information Services in Astronomy V, eds. S. Ricketts, C. Birdie, & E. Isaksson, ASP Conf. Ser., 377, 197
Whitaker, K. E., Franx, M., Leja, J., et al. 2014, ApJ, 795, 104
Xia, L., Malhotra, S., Rhoads, J., et al. 2011, AJ, 141, 64
Xu, C., Pirzkal, N., Malhotra, S., et al. 2007, AJ, 134, 169
Xue, Y. Q., Wang, S. X., Brandt, W. N., et al. 2012, ApJ, 758, 129

Pages 14 to 17 are available in the electronic edition of the journal at http://www.aanda.org

Table 1. 40 objects in our statistically complete "basic sample".

ID	RA and Dec	*NB*	*NB* − *Y*	*NB* − *J*	Redshift	*z*[Peak]	*z*[min/max]	Line ID	Em. line flux	Eq. width	Ref.
ELG#	(2000.0)	mag (AUTO)	mag (ISO)	mag (ISO)	This work	MUSYC	MUSYC		[10^{-17} erg/s/cm^2]	Å	
03	03:32:40.32 −27:47:22.71	22.11 ± 0.01	−0.61 ± 0.01	−0.80 ± 0.02	0.619	0.61	0.60/0.63	Hα	17.54 ± 0.14	188.3 ± 2.0	(1)
04	03:32:44.30 −27:46:59.99	23.60 ± 0.03	−0.62 ± 0.03	−1.16 ± 0.09	1.144	1.12	1.10/1.14	[OIII]	9.03 ± 0.13	288.1 ± 9.1	(2)
05	03:32:36.30 −27:47:32.63	23.43 ± 0.02	−1.20 ± 0.03	−0.96 ± 0.06	1.86	2.29	2.05/2.48	[OII]	28.55 ± 0.12	533.8 ± 11.3	(3)
06	03:32:37.20 −27:47:25.56	23.88 ± 0.06	−0.70 ± 0.07	−0.43 ± 0.11	1.85	–	–	[OII]	13.28 ± 0.22	405.5 ± 25.7	
09	03:32:41.34 −27:46:46.23	24.27 ± 0.05	−0.55 ± 0.05	−0.64 ± 0.10	0.62	0.60	0.56/0.64	Hα	1.98 ± 0.08	155.3 ± 8.2	
10	03:32:37.97 −27:46:51.86	21.03 ± 0.01	−0.71 ± 0.01	−0.90 ± 0.01	0.62	0.63	0.62/0.63	Hα	43.86 ± 0.41	235.8 ± 2.5	(4)
11	03:32:42.76 −27:46:33.19	24.45 ± 0.05	−0.81 ± 0.06	−0.99 ± 0.14	0.62	0.64	0.62/0.66	Hα	1.65 ± 0.08	201.2 ± 10.6	
12	03:32:37.36 −27:46:45.52	21.91 ± 0.01	−0.85 ± 0.01	−0.43 ± 0.02	1.843	2.26	2.22/2.31	[OII]	155.23 ± 0.19	257.3 ± 2.7	(5)
14	03:32:36.83 −27:46:51.52	24.51 ± 0.06	−0.88 ± 0.08	−0.65 ± 0.13	1.85	1.80	1.72/1.89	[OII]	2.85 ± 0.08	153.6 ± 9.7	
15	03:32:37.08 −27:46:47.03	23.10 ± 0.02	−1.03 ± 0.03	−0.93 ± 0.06	1.85	1.93	1.84/2.04	[OII]	24.09 ± 0.13	287.1 ± 6.1	
16	03:32:35.81 −27:46:43.62	23.26 ± 0.03	−0.79 ± 0.03	−0.32 ± 0.04	1.85	2.13	1.88/2.32	[OII]	21.17 ± 0.13	163.8 ± 5.2	(6)
20	03:32:36.69 −27:46:20.98	23.74 ± 0.02	−0.90 ± 0.04	−0.99 ± 0.08	1.85	1.90	1.80/2.00	[OII]	9.42 ± 0.07	234.3 ± 5.0	(3)
21	03:32:37.45 −27:46:15.34	24.55 ± 0.07	−0.79 ± 0.07	−0.64 ± 0.12	1.85	1.94	1.83/2.04	[OII]	4.52 ± 0.09	141.6 ± 10.5	
22	03:32:36.55 −27:46:12.28	22.60 ± 0.01	−0.93 ± 0.02	−0.79 ± 0.04	1.85	1.94	1.90/1.98	[OII]	53.91 ± 0.11	351.3 ± 3.7	(3)
23	03:32:39.52 −27:45:59.75	24.59 ± 0.08	−1.13 ± 0.11	−0.99 ± 0.20	1.85	1.86	1.43/2.31	[OII]	6.32 ± 0.14	314.9 ± 26.7	
25	03:32:39.33 −27:45:55.14	23.38 ± 0.04	−1.21 ± 0.05	−0.96 ± 0.08	1.85	1.90	1.75/2.04	[OII]	22.05 ± 0.24	474.7 ± 20.1	
26	03:32:45.73 −27:45:24.97	23.72 ± 0.04	−0.71 ± 0.04	−0.80 ± 0.08	1.15	1.09	1.05/1.12	[OIII]	5.29 ± 0.12	178.7 ± 7.6	
28	03:32:27.82 −27:46:35.07	24.02 ± 0.03	−1.31 ± 0.05	−1.67 ± 0.16	1.15	–	–	[OIII]	6.50 ± 0.11	699.8 ± 22.2	
30	03:32:30.03 −27:46:04.24	24.35 ± 0.05	−1.59 ± 0.09	−3.08 ± 0.61	1.15/1.85/0.62	–	–	[OIII]/[OII]/Hα	2.96 ± 0.16	1851.6 ± 97.9	
34	03:32:26.60 −27:46:05.02	24.76 ± 0.08	−0.77 ± 0.09	−1.14 ± 0.22	1.15	1.28	1.06/1.55	[OIII]	1.38 ± 0.12	294.7 ± 24.9	
35	03:32:21.53 −27:46:18.71	23.31 ± 0.03	−0.80 ± 0.03	−0.57 ± 0.06	1.85	1.74	1.50/1.96	[OII]	29.74 ± 0.19	420.8 ± 13.4	
36	03:32:26.68 −27:45:54.79	23.98 ± 0.04	−1.12 ± 0.05	−1.43 ± 0.13	1.15	1.18	1.09/1.30	[OIII]	4.60 ± 0.15	566.7 ± 24.0	
37	03:32:21.69 −27:46:16.57	24.70 ± 0.07	−1.01 ± 0.08	−0.57 ± 0.12	1.85	2.45	2.32/2.59	[OII]	4.16 ± 0.10	274.7 ± 20.3	
41	03:32:21.26 −27:46:02.55	23.68 ± 0.03	−0.93 ± 0.04	−0.82 ± 0.07	1.85	1.53	1.12/1.74	[OII]	8.11 ± 0.11	272.6 ± 8.7	
43	03:32:19.60 −27:46:08.31	23.63 ± 0.03	−0.61 ± 0.03	−1.08 ± 0.09	1.15	1.07	1.05/1.09	[OIII]	5.43 ± 0.16	683.2 ± 21.7	
45	03:32:42.51 −27:44:15.55	23.38 ± 0.03	−0.66 ± 0.03	−0.77 ± 0.06	0.62	0.61	0.60/0.63	Hα	4.73 ± 0.12	169.6 ± 5.4	
51	03:32:16.50 −27:44:45.04	22.49 ± 0.02	−0.53 ± 0.02	−0.76 ± 0.04	1.15/0.62	1.11	1.10/1.12	[OIII]/Hα	19.61 ± 0.31	809.5 ± 17.1	
52	03:32:41.59 −27:42:50.68	24.62 ± 0.08	−0.35 ± 0.08	−0.93 ± 0.18	1.15	–	–	[OIII]	1.44 ± 0.12	238.3 ± 20.2	
53	03:32:13.15 −27:45:01.19	23.18 ± 0.02	−0.91 ± 0.03	−0.41 ± 0.04	1.85	2.06	1.95/2.17	[OII]	27.63 ± 0.12	249.4 ± 5.3	
54	03:32:12.98 −27:44:59.81	23.16 ± 0.02	−0.89 ± 0.03	−0.80 ± 0.05	1.85	–	–	[OII]	35.58 ± 0.15	476.8 ± 10.1	
55	03:32:16.31 −27:44:41.93	22.03 ± 0.01	−0.56 ± 0.01	−0.77 ± 0.02	1.1107	1.12	1.11/1.12	[OIII]	43.90 ± 0.14	159.8 ± 1.7	(*)
58	03:32:41.68 −27:42:04.45	23.50 ± 0.03	−1.04 ± 0.04	−1.16 ± 0.10	1.15/1.85	1.25	1.21/1.30	[OIII]/[OII]	4.81 ± 0.15	384.9 ± 12.2	
62	03:32:34.22 −27:42:31.37	24.37 ± 0.04	−1.10 ± 0.07	−1.83 ± 0.25	0.62	0.61	0.60/0.63	Hα	1.90 ± 0.07	202.4 ± 8.6	
65	03:32:39.20 −27:41:44.69	23.05 ± 0.02	−1.12 ± 0.03	−1.55 ± 0.08	1.15	1.14	1.12/1.15	[OIII]	9.54 ± 0.17	546.4 ± 11.6	
66	03:32:38.22 −27:41:45.51	24.31 ± 0.07	−0.92 ± 0.11	−0.87 ± 0.21	1.85/1.15	–	–	[OII]/[OIII]	5.67 ± 0.19	545.0 ± 40.4	
68	03:32:23.88 −27:42:11.56	24.07 ± 0.05	−0.65 ± 0.05	−0.57 ± 0.09	1.85	1.60	1.50/1.70	[OII]	3.94 ± 0.12	219.5 ± 11.6	
70	03:32:33.03 −27:40:48.06	23.14 ± 0.02	−0.56 ± 0.02	−0.83 ± 0.06	1.15	1.13	1.11/1.14	[OIII]	7.26 ± 0.10	174.9 ± 3.7	
75	03:32:30.36 −27:41:46.66	24.37 ± 0.06	−0.94 ± 0.07	−0.56 ± 0.10	1.85/1.15	–	–	[OII]/[OIII]	5.99 ± 0.13	321.0 ± 20.4	
76	03:32:22.75 −27:42:11.59	23.17 ± 0.02	−0.76 ± 0.03	−0.45 ± 0.04	1.85	1.89	1.76/2.00	[OII]	28.31 ± 0.12	258.4 ± 5.5	
78	03:32:33.89 −27:42:37:92	20.13 ± 0.01	−0.73 ± 0.01	−0.74 ± 0.01	0.624	0.64	0.64/0.65	Hα	183.81 ± 0.90	210.9 ± 2.2	(7)

Notes. In the first column, we present our ID numbers for the candidate emission-line galaxies. Next we list RA & Dec, NB magnitudes, colours and redshift from our work accordingly. In Cols. 7 and 8 we present redshifts reported in the MUSYC catalogue: *z*[peak] corresponds to the best assigned redshift by the survey and [zmin] and [zmax] represent 1σ minimum and maximum redshift values. Column 9 lists the emission lines observed in the narrow-band filter; here [OIII] means [OIII]/Hβ. For 5 objects we could not uniquely assign a redshift; for four of them we have preferred value, which is listed first, while for ELG30 we do not have a preferred redshift identification and we consider all the three listed values possible. Column 10 lists emission-line fluxes and Cols. 11 and 12 corresposnd to the observed frame equivalent width and references to the spectroscopic redshift literature, respectively.

References. (1) Ravikumar et al. (2007); (2) Xu et al. (2007); (3) Trump et al. (2011); (4) Rodrigues et al. (2008); (5) Mignoli et al. (2005); (6) Guo et al. (2012); (*) this work; (7) Balestra et al. (2010).

Table 2. Continuation of Table 1 with candidates from the extended sample.

ID	RA and Dec	Redshift	line ID	NB	$NB - Y$	$NB - J$	Em.line flux	Eq. width	Ref.
	(2000.0)	spectroscpic		mag (AUTO)	mag (ISO)	mag (ISO)	[10^{-17} erg/s/cm^2]	Å	
ELG00	03:32:18.57 −27:42:29.50	0.6045	Hα	22.46 ± 0.01	−0.10 ± 0.01	−0.55 ± 0.02	5.07 ± 0.05	69.6 ± 0.7	(*)
x01	03:32:13.24 −27:42:40.03	0.6072	Hα	18.88 ± 0.01	−0.36 ± 0.01	−0.35 ± 0.01	227.56 ± 0.21	152.8 ± 0.1	(1)
x02	03:32:23.40 −27:43:16.58	0.615	Hα	19.72 ± 0.01	−0.47 ± 0.01	−0.29 ± 0.01	98.15 ± 0.16	135.4 ± 0.2	(2)
x03	03:32:41.83 −27:40:42.31	0.6162	Hα	23.35 ± 0.02	−1.29 ± 0.04	−1.78 ± 0.13	6.50 ± 0.16	721.0 ± 17.8	(1)
x04	03:32:38.59 −27:46:31.36	0.625	Hα	20.87 ± 0.01	−0.31 ± 0.01	−0.27 ± 0.01	25.03 ± 0.13	83.4 ± 0.4	(3)
x05	03:32:31.50 −27:41:58.04	0.620	Hα	23.32 ± 0.02	−0.32 ± 0.02	−0.27 ± 0.03	2.48 ± 0.05	77.0 ± 1.6	(1)
x06	03:32:45.65 −27:44:05.80	0.6206	Hα	20.15 ± 0.01	−0.41 ± 0.01	−0.39 ± 0.01	63.40 ± 0.17	127.7 ± 0.3	(1)
x07	03:32:28.01 −27:43:57.44	0.6207	Hα	21.93 ± 0.01	−0.53 ± 0.01	−0.78 ± 0.03	12.70 ± 0.16	133.4 ± 1.7	(4)
x08	03:32:40.79 −27:46:15.70	0.6218	Hα	19.57 ± 0.01	−0.36 ± 0.01	−0.31 ± 0.01	85.02 ± 0.20	86.6 ± 0.2	(1)
x09	03:32:46.75 −27:46:24.02	0.6250	Hα	24.86 ± 0.06	−0.78 ± 0.06	−1.12 ± 0.16	0.98 ± 0.07	169.8 ± 11.5	(5)
x10	03:32:22.25 −27:49:01.47	1.109	[OIII]	22.98 ± 0.02	−0.19 ± 0.02	−0.22 ± 0.03	2.09 ± 0.04	41.3 ± 0.8	(6)
x11	03:32:27.66 −27:45:05.77	1.110	[OIII]	23.02 ± 0.02	−0.22 ± 0.02	−0.34 ± 0.04	3.55 ± 0.09	86.8 ± 2.2	(6)
x12	03:32:26.77 −27:45:30.63	1.122	[OIII]	22.97 ± 0.02	−0.69 ± 0.02	−1.00 ± 0.06	7.11 ± 0.17	290.4 ± 6.8	(6)
x13	03:32:18.81 −27:49:08.59	1.128	[OIII]	23.19 ± 0.02	−0.46 ± 0.02	−0.91 ± 0.05	4.66 ± 0.10	177.2 ± 3.7	(7)
x14	03:32:49.83 −27:46:58.30	1.174	Hβ	24.70 ± 0.06	−1.05 ± 0.08	−1.33 ± 0.21	1.44 ± 0.09	293.3 ± 17.8	(1)
x15	03:32:17.11 −27:42:20.95	1.749	[NeIII]	24.52 ± 0.05	−0.47 ± 0.05	−0.65 ± 0.10	0.51 ± 0.03	41.2 ± 2.2	(8)
x16	03:32:38.80 −27:47:14.82	1.836	[OII]	22.67 ± 0.02	−0.65 ± 0.02	−0.08 ± 0.02	8.17 ± 0.16	209.6 ± 4.0	(9)
x17	03:32:18.43 −27:42:51.95	1.846	[OII]	25.08 ± 0.09	−0.53 ± 0.09	−0.18 ± 0.13	0.56 ± 0.05	93.5 ± 9.2	(8)
x18	03:32:36.69 −27:46:48.48	1.86	[OII]	24.60 ± 0.07	−0.47 ± 0.06	−0.17 ± 0.09	0.91 ± 0.07	101.8 ± 7.9	(10)

Notes. Column 1: ID number, Col. 2: coordinates of the objects. Redshift and line IDs are listed in third and fourth columns respectively. Column 5 lists narrow-band magnitudes and magnitude errors. Columns 6 and 7 present colors and color errors for Y and J filters respectively. And final three columns are emission-line fluxes, observed frame equivalent widths, and references to the literature where we obtain spectroscopic redshift.

References. (*) This work; (1) Balestra et al. (2010); (2) Vanzella et al. (2005); (3) Szokoly et al. (2004); (4) Le Fèvre et al. (2004); (5)Xia et al. (2011); (6) Vanzella et al. (2006); (7) Villforth et al. (2012); (8) Straughn et al. (2011); (9) Guo et al. (2012); (10) Trump et al. (2011).

Appendix A: Thumbnail images for the "basic sample" galaxies

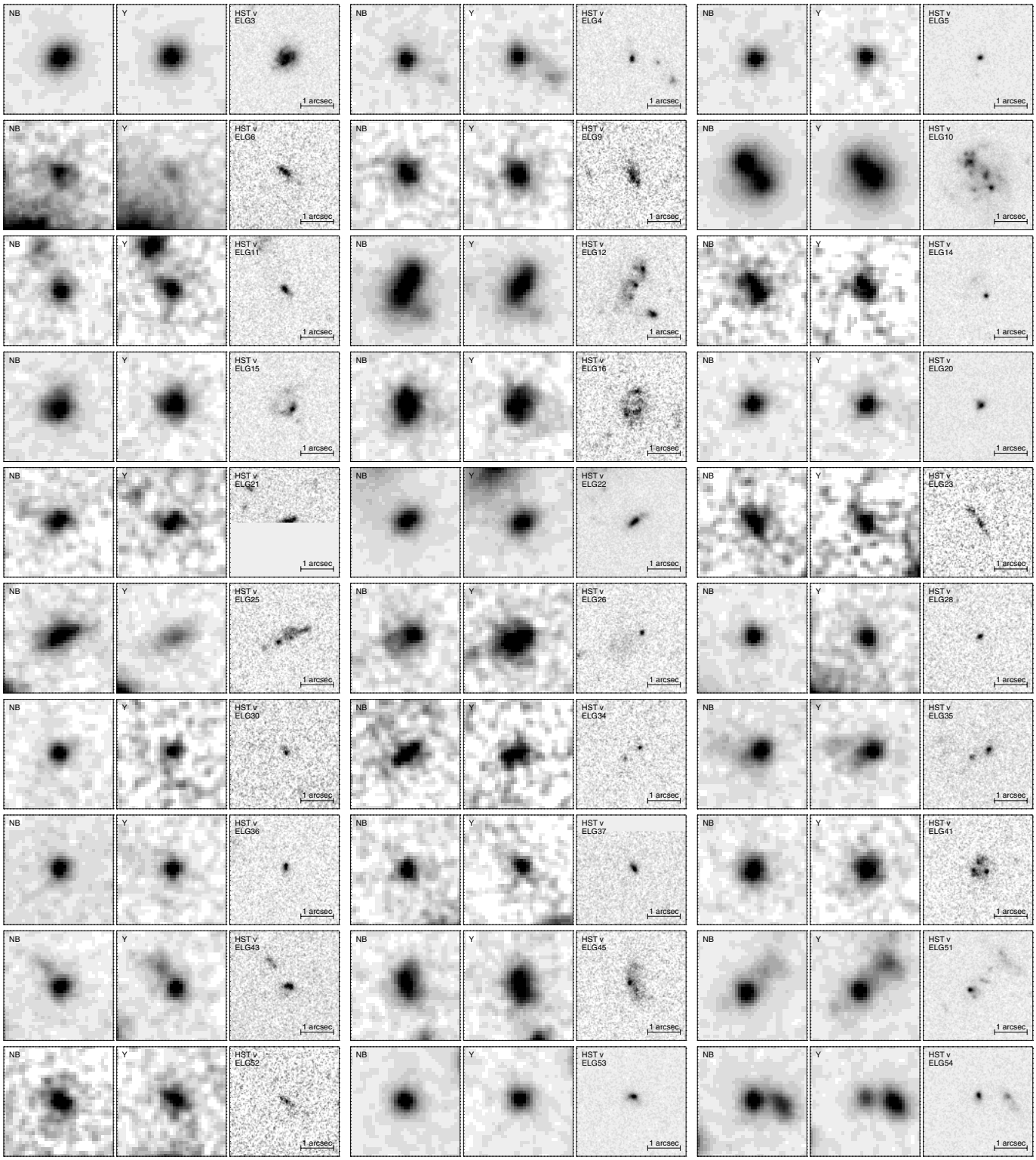

Fig. A.1. Thumbnail images of the $NB1060$, Y, and HST $F606W$ ("v band") filters for the candidates selected from $NB1060 - Y$ and $NB1060 - J$ colours and the additional source (ELG00) only detected including the $NB1060 - J$ colour. A 1″ bar is given on the panels.

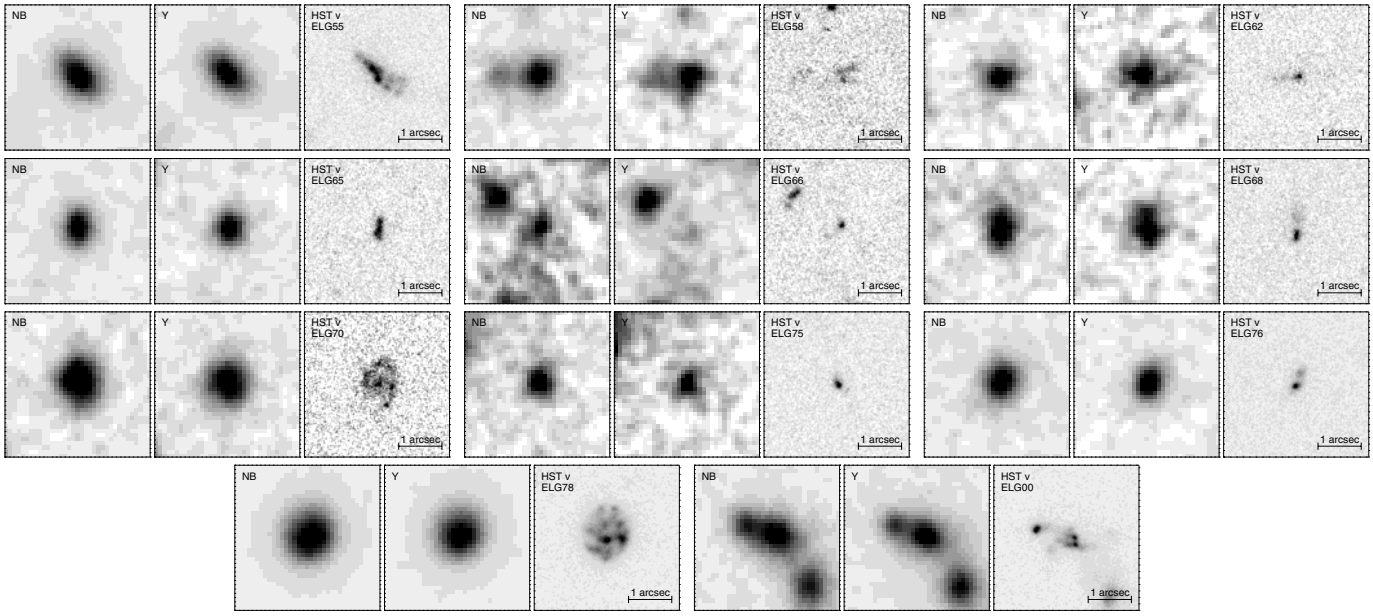

Fig. A.1. continued.